People's Democratic Republic of Algeria

Ministry of Higher Education and Scientific Research

University of Echahid Cheikh Larbi Tebessi-Tebessa

DOCTORAL THESIS

3rd cycle Doctorate in

Condensed Matter Physics

By

Guenez Wafa

STUDY OF STRUCTURAL, ELECTRONIC, AND MAGNETIC PROPERTIES OF RARE-EARTH-BASED DOUBLE PEROVSKITES

Date: [redacted]

Jury Members

Chairperson	Serdouk Fadila	MCA	Echahid Cheikh Larbi Tebessi, Tebessa University
Supervisor	Chemam Faïçal	Prof	Echahid Cheikh Larbi Tebessi, Tebessa University
Examiner	Azzouzi Fayçal	Prof	Mohamed Cherif Messaadia, Souk Ahras University
Examiner	Chaouche Yassine	MCA	Echahid Cheikh Larbi Tebessi, Tebessa university
Examiner	Mimouni Mourad	MCA	Echahid Hamma Lakhdar, El-Oued, University
Examiner	Zaouai Souhila	MCA	Echahid Cheikh Larbi Tebessi, Tebessa University
Guest	Bouguerra Abdesselam	MCA	Mohamed Cherif Messaadia, Souk Ahras University

2023/2024

Acknowledgments

My sincere gratitude extends to Prof. **Chemam Faïçal** from the University of Tebessa, who directed my thesis, for his support and encouragement throughout the years, particularly regarding the handling of my thesis topic. I am grateful for his availability throughout these five years of thesis work and for all the advice and discussions we have had with a positive attitude.

I would like to express my heartfelt gratitude to Dr. **Serdouk Fadila** for graciously accepting the role of chairing the defense committee. I am also thankful to Prof. **Azzouzi Fayçal**, Dr. **Mimouni Mourad**, Dr. **Chaouche Yassine** and Dr. **Zaouai Souhila** for agreeing to evaluate my research work. Grateful to the Dr. **Bouguerra Abdesselam** for his participation in our collaborative article. He was truly instrumental in shaping the research and enhancing its quality. Thank you for your presence at my graduation ceremony.

Under the direction of Prof. **Chemam Faïçal**, this thesis was completed at the Laboratory of Applied and Theoretical Physics (LPAT), Cheikh Larbi Tebessi University, Faculty of Exact and Natural Sciences, Tebessa.

Allhamdulillah

I dedicate this work to my Mama and Baba.... my brothers (Ahmed, Nassim and Abderahmane) ..... my dear sister Amira, and my close friends(Moni, Dodi, Assia, Ahd).

ABSTRACT

This study aimed to explore the potential uses of new double perovskite oxides, which show promise as functional materials for high-density storage and optoelectronic applications. Our approach involved using first-principle calculations to examine the physical properties of these materials and gain a deeper understanding of their potential applications. Specifically, we focused on double perovskites based on rare earths, such as Ba_2RERuO_6 (RE= Er, Tm, Gd) and investigated their physical properties, including magnetic, structural, electronic, magneto-optical, and optical properties. To analyze these properties, we utilized the density functional theory (DFT) concept and employed the full-potential linearized augmented plane wave method (FP-LAPW). Initially, the optimized unit cell structure of three compounds shows a ferromagnetic cubic form with a space group of $Fm\bar{3}m$. The electronic findings of Ba_2GdRuO_6 for GGA and GGA+U indicate a semiconductor nature. The high magnetism associated with the $4f$ of rare earth elements and the $4d$ of transition metals gives rise to the ferrimagnetic phase. Moreover, the optical properties of Ba_2GdRuO_6 exhibit ideal optical conductivity and an efficient absorption coefficient within the visible and ultraviolet range of electromagnetic radiation. The potential of this newly created material as a candidate for optoelectronic devices is promising. In the case of the second set of compounds, the (GGA + U) calculation showed that Ba_2TmRuO_6 is a half-metallic compound, while Ba_2ErRuO_6 is a semiconductor compound. For Ba_2ErRuO_6 and Ba_2TmRuO_6, the magneto-optical findings show giant peaks of the Kerr effect (MOKE) displayed at angles around 17.7° and 5.6°, respectively, approximately 0.2 eV. Respectively, these results indicate their potential applications in the infrared and UV regions.

RESUME

L'objectif de cette étude était d'explorer les utilisations potentielles des nouveaux oxydes de double perovskite, qui offrent des perspectives prometteuses en tant que matériaux fonctionnels pour le stockage à haute densité et les applications optoélectroniques. Nous avons adopté une approche basée sur des calculs de premiers principes pour étudier les propriétés physiques de ces matériaux. Nous nous sommes concentrés sur les double perovskites à base de terres rares Ba_2RERuO_6 (RE = Er, Tm, Gd) et avons exploré leurs propriétés structurelles, magnétiques, électroniques, optiques et magnéto-optiques en utilisant la méthode de plan d'onde augmentée linéarisée (FP-LAPW) dans le cadre de la théorie de la fonctionnelle de la densité (DFT). Les propriétés magnéto-optiques, y compris les effets spin-orbite attribuables aux électrons Ru-4d et RE-4f, ont été calculées en utilisant les approximations du gradient généralisé (GGA) et du GGA+U.

La structure optimisée de la maille cristalline de trois composés présente une forme cubique ferrimagnétique avec un groupe d'espace Fm-3m. Les résultats électroniques de Ba_2GdRuO_6 obtenus avec les méthodes GGA et GGA+U indiquent une nature semi-conducteur. De plus, les propriétés optiques de Ba_2GdRuO_6 ont montré une conductivité optique idéale et un coefficient d'absorption efficace dans la région du rayonnement électromagnétique visible et ultraviolet.

Dans le cas du deuxième ensemble de composés, le calcul (GGA+U) a montré que Ba_2TmRuO_6 était semi-métallique, tandis que Ba_2ErRuO_6 était un semi-conducteur avec une énergie de bande interdite directe pour les deux composés. L'effet Kerr magnéto-optique (MOKE) a révélé des pics à des angles d'environ 17.7º et 5.6º autour de 0.2 eV pour Ba_2ErRuO_6 et Ba_2TmRuO_6, respectivement, indiquant leur potentiel d'application dans les régions infrarouge et UV.

En résumé, notre recherche offre des perspectives précieuses sur les applications potentielles des oxydes de double pérovskite et souligne l'importance de comprendre leurs propriétés physiques grâce à des calculs de première-principes.

ملخص

إن الهدف من هذه الدراسة هو تحديد استخدامات أكسيد البيروفسكيت المزدوج، التي اظهرت خصائص واعدة كمواد قابلة للتخزين عالي الكثافة وكذلك تطبيقاتها في الاجهزة الإلكترونية البصرية. تتضمن طريقة العمل على استخدام نظرية المبدأ الأول (DFT) لفحص الخصائص الفيزيائية لهذه المواد وفهم أفضل لتطبيقاتها المحتملة. تركز دراستنا بشكل خاص على أكسيدات البيروفسكيت مزدوجة المعتمدة اساسا على عناصر الأرض النادرة (Ba_2RERuO_6 (RE = Er,Tm, Gd واكتشاف خصائصها البنيوية ،المغناطيسية، الإلكترونية، المغناطسية الضوئية باستخدام طريقة الامواج المستوية المتزايدة خطيا مع وجود الكمون الكامل (FP-LAPW) في إطار نظرية الكثافة الوظيفية DFT و الذي تم علاج كمون التبادل-الترابط بتقريب GGA و GGA+U.

في البداية، وجدنا ان بنية خلية الوحدة لهذه المركبات ذات بنية مكعبة ذات فضاء المجموعة (Fm-3m) مع استقرارهم في طور ضد فيرمغناطيسي (FIM) و أيضا أشارت النتائج ان المركب Ba_2GdRuO_6 ذي سلوك شبه موصل، حيث ان قيم الفجوة الطاقية للتقريبات GGA و GGA+U هي eV1.024, و eV 1.316 على التوالي. علاوة على ذلك، أظهرت الخواص البصرية لمركب Ba_2GdRuO_6 توصيلًا ضوئيا عاليًا بقيمة ($\Omega^{-1}cm^{-}10^{5}$ [1]) وثوابت عزل عالية، ومعامل امتصاص للضوء قوي في الطيف الكهرومغناطيسي المرئي و ما فوق البنفسجيةUV.

فيما يتعلق بالمجموعة الثانية من المركبات $Ba_2B'RuO_6$ ، أظهر حساب (GGA + U) أن Ba_2TmRuO_6 هو شبه معدن، فيما اظهر Ba_2ErRuO_6 هو الاخر سلوك شبه ناقل ويمتلك فجوة طاقية مباشرة لكلا المركبين. أظهرت ظاهرة Kerr للخاصية المغناطسية الضوئية، ذروات عند زوايا حوالي ° 17.7 و °5.6 عند قيمة eV 0.2 لكل من Ba_2ErRuO_6 و Ba_2TmRuO_6 على التوالي، مما يشير إلى إمكانية تطبيقاتها في المنطقة المجاورة للأشعة تحت الحمراء وفوق البنفسجية.

في الخلاصة، تقدم بحثنا نظرة قيمة على الاستخدامات المحتملة لأكاسيد ثنائية بيروفسكايت ويؤكد على أهمية فهم خصائصها الفيزيائية من خلال حسابات المبادئ الأولى.

List of Figures

List of Tables

Contents

GENERAL INTRODUCTION

Double perovskite oxides have recently demonstrated significant potential for various industrial and technical applications due to their distinctive physical and chemical properties. Examples of these applications include photovoltaic devices, spintronic devices, and magneto-optical devices [1–12]. The challenge of meeting the demand for clean energy is a pressing issue in contemporary times. Solar energy, a crucial power source in photovoltaic devices, has driven researchers to explore novel materials that are cost-effective, environmentally friendly, and possess superior optical properties. In this context, perovskite materials have emerged as a promising area of investigation [13–15]. Recent research has delved into double perovskite oxides comprising both transition metals (TM) and rare earth (RE) elements. The incorporation of lanthanide elements (Eu, Dy, Tm, Yb) in perovskite materials as photo-absorbing compounds holds significant promise in solar cells, as evidenced by predicted band gap values ranging between 2.0 and 3.2 eV. Pazoki et al. conducted a study on the electronic structures of various organometallic perovskites based on rare earths. Additionally, the notable visible-range features of A_2NiMnO_6 (A = La, Sm) make it an excellent candidate for use in solar cells and photocatalyst applications [16–18]. Double perovskite materials, such as $Ca_2BB'O_6$ (with B = Y, Gd, La and B′ = Nb, Sb, Ta) and $Ba_2GdB'O_6$ (with B′ = Nb, Sb), have been identified as luminescent materials with potential applications in white light-emitting devices.

Moreover, it is widely recognized that these compounds possess unique characteristics of interest due to their structural and physical properties being highly sensitive to minor modifications in their chemical composition. For instance, the substitution of A and B cations can result in different crystal structures, as evidenced by the investigation of A_2REMO_6 materials (where A= Sr, Ba, and Ca) containing rare earth (RE) and transition metal element (M) [19–21]. The double perovskites with Ba as the A-cation have been noted to assume face-centred cubic (FCC) lattices with the space group (Fm=3m) [22, 23]. The double perovskite material, known as A_2GdRuO_6, possesses a monoclinic crystal symmetry with a space group of (P21/n) [24]. However, the structure of this compound is slightly distorted from its ideal form due to the mismatch in ionic radii between the A cation and the average B cation. This distortion can be attributed to the larger ionic radius of Ba cations compared to Sr cations, as observed in

Sr_2RuHoO_6 [25]. To determine the crystal structure of A_2GdRuO_6 compounds, X-ray diffraction analysis was conducted. The results showed that the double perovskite compound with barium (Ba) had a cubic crystal structure, whereas the crystal structure of Sr_2GdRuO_6 was monoclinic [26]. The structural composition of double perovskites can be altered in response to changes in pressure and temperature, resulting in diverse characteristics such as metallic, insulating, half-metallic (HM), or semiconducting [27–31]. The category of half-metallic materials (HM) displays distinct characteristics, demonstrating properties that lie between those of metals and semiconductors in both spin-up and spin-down channels. This exceptional characteristic is defined by a resilient spin polarization that can achieve percentages as elevated as 100%. [32]. Numerous oxides comprising rare earth (RE) elements with 4f orbitals and transition metals (TM) with 4d or 5d orbitals exhibit the characteristic of being HM. These materials are considered to possess consistent magnetic orderings, facilitating the formation of diverse magnetic phases. Kumar et al. [33] have reported that Ba_2YbTaO_6 exhibits a half-metallic ferromagnetic character with significant optical properties. Theoretical studies have also been conducted on Ba_2LnTaO_6 (Er, Tm) to demonstrate their half-metallic paramagnetic nature [34]. Haid et al. [22, 23] have investigated the effect of U potential on the half-metallic ferromagnetic material of Ba_2REReO_6 (RE= Ho, Er) through theoretical analysis [29].

The phenomenon of the rotation of reflected light from a magnetized surface is commonly referred to as the magneto-optical Kerr effect (MOKE) [35]. The search for materials exhibiting a Kerr rotation greater than or equal to 0.2°, considered valuable in MO storage devices, remains an active area of research.For example, $Sr2FeWO6$ exhibits Kerr rotation values of 3.87° at 1.55 eV [4], while Ba_2NiOsO_6 demonstrates a Kerr rotation of 6° at 3.2eV [7]. In the case of the ferromagnetic perovskite $BiNiO_3$, the Kerr rotation is 1.28° at 1.87eV [36]. Recently, Zu et al. [37] reported the use of $Sr_2BB^{'}O_6$ (B = Cr, Mo; B' = W, Re, Os) and found that the Kerr effect value reaches $-5.02°$ in the infrared to the visible light spectrum.

Density Functional Theory (DFT) is a cost-effective method that can be utilized to predict the properties of a new compound, surpassing the need for experimental procedures. In essence, the DFT approach serves as a primary means of determining the characteristics of materials [38].

The research we present in our thesis centers around the double perovskites Ba_2RERuO_6. Despite their theoretical significance, these materials have received scant attention in existing literature. To address this gap, we have conducted first-principle calculations to determine their structural, electronic, magnetic, optical, and magneto-optical properties for the RE elements Gd, Er, and Tm.

The present thesis manuscript is organized as follows:

► The introductory chapter provides a comprehensive overview of double perovskite materials.

► The second chapter comprises two initial sections. The first section provides a brief explanation of the first principle calculation, namely Density Functional Theory (DFT). The second section delves into the primary method employed in this thesis, namely the Full Potential Linearized Augmented Plane Wave (FP-LAPW) method.

► The third chapter presents the outcomes of the discussion.

► The final section of this study presents a comprehensive summary of the most noteworthy findings, thereby highlighting the overall conclusion.

Chapter 1

DOUBLE PEROVSKITE OXIDES MATERIALS

- **An Overview of the Perovskite Family.**
- **Double perovskite materials and their properties.**
- **Some application of double perovskite.**

1.1 Introduction

Perovskites are a group of crystalline oxides that can be classified in many different ways, as shown in Figure (1.1). The mineral $CaTiO_3$ was discovered by Russian mineralogist G. Rose in 1839, and was named "Perovskite" after Russian mineralogist V. Perovski. The general chemical structure of these minerals is represented as ABX_3, where A cations can be alkaline earth or rare earth, B cations are transition metals of varying sizes, and X denotes anions such as O^{2-}, F^{-}, S^{2-}, or halogen elements. Depending on the nature of the cations A and B, various combinations are possible, as illustrated in Equation (1.1.1). This principle guides the identification of different materials based on the valence states of these cations [1].

$$Q_A + Q_B = -3Q_X \tag{1.1.1}$$

Where the combinations of perovskite depends on the oxidation states of each ion[39]:

- $Q_A = 1$; $Q_B = 2$; $Q_X = -1$; $KMgF_3$, $KZnF_3$, and $AgMgF_3$[40]
- $Q_A = 2$; $Q_B = 4$; $Q_X = -2$; AMS_3; A = (Ba, Ca, Sr); M = (Hf, Sn) [41]
- $Q_A = 1$; $Q_B = 5$; $Q_X = -2$; $KNbO_3$, $NaNbO_3$ [42]
- $Q_A = 4$; $Q_B = 5$; $Q_X = -3$; $LaReN_3$, $LaWN_3$, and $YReN_3$[43]

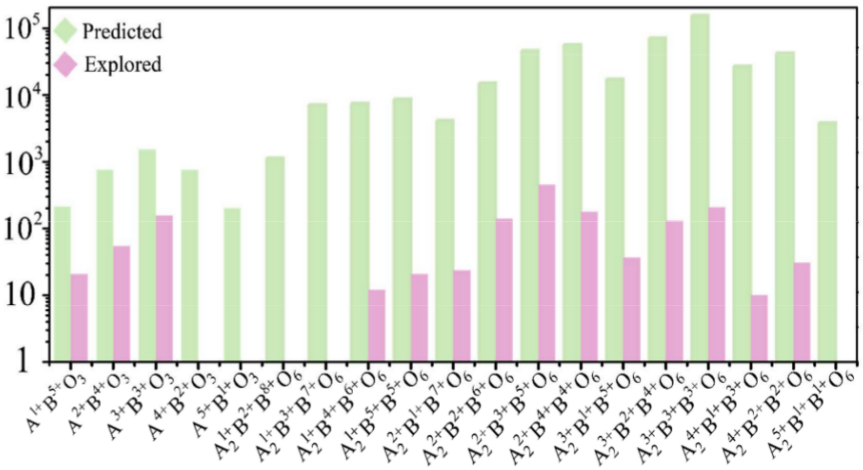

Figure 1.1: Various compositional forms of perovskite structures[1].

1.2 Single perovskite structure

The perovskite oxide family is renowned for its characteristic crystallographic structure. This distinctive feature is a result of the arrangement of atoms in a cubic unit cell, with a central cation surrounded by six octahedrally coordinated anions. This unique structure has piqued the interest of researchers due to its potential applications in a wide range of fields, including electronics, energy storage, and catalysis. A thorough understanding of the crystallographic properties of perovskite oxides is crucial for the development of new materials and the optimization of existing ones. The ideal structure of the material is cubic with a symmetry group of Pm=3m (221) as illustrated in Figure (1.2-(a)) using Miller representation forms [44]. In crystal structures, A cations are typically found at the corners of a cube, with coordinates (0, 0, 0), surrounded by twelve anions (X) in an octahedral coordination. Conversely, B cations usually occupy the centre of the cube, with coordinates (0.5, 0.5, 0.5), surrounded by six anions. In addition, the X anions are located at the centre of each face of the cube, with coordinates (0.5, 0.5, 0), surrounded by 2B cations and 4A cations. When the cubic structure is replicated, it produces a network that is similar to the one shown in the second form of the Miller representation. In this configuration, the A cation is placed at the centre of the cube with coordinates $(0.5, 0.5, 0.5)$, and the B cation is located at the corners of the cube at coordinates $(0, 0, 0)$. The X anions are positioned in the middle of the edges of the cube and have coordinates $(0.5, 0, 0)$. This arrangement is visually represented in Figure (1.2)-(b) [45].

1.2.1 The Tolerance Factor

In 1928, Goldschmidt conducted a study on the stability of perovskite structures. He used geometric criteria to determine whether perovskite materials will have a cubic or distorted structure. This method is still used today. Goldschmidt established a dimensional parameter called the tolerance factor (t) by considering the ratios of ionic radii. This factor helps to estimate the degree of distortion in the crystal structure.

The tolerance factor is calculated based on the ionic radii ratios and serves as an indicator of the deviation from the ideal cubic structure. In the ideal cubic arrangement, the

distance between ions B and O is denoted as $\frac{a}{2}$. Simultaneously, the distance between ions A and O is $\frac{a}{\sqrt{2}}$ units, establishing a specific relationship between the A and B radii, as expressed by the Goldschmidt factor in the following equation:

$$t = \frac{(r_A + r_X)}{\sqrt{2}(r_B + r_X)} \tag{1.2.1}$$

Here, r_A, r_B, and r_X represent the ionic radii of A, B, and X, respectively. The perovskite structure remains stable within the specified range of 0.78 < t < 1.05. The cubic form is favoured when the tolerance factor falls between 0.95 and 1.05. Additionally, this factor provides insights into the vast array of substitutions observed at sites A and B.

► If $t < 1$, a small cation radius at the A site minimizes A-O distances, inducing coordination reduction and BO_6 octahedral tilting.

► If $t > 1$, the cuboctahedral cavity of the octahedron is filled by the excessively massive A cation. The ideal perovskite's octahedral shape distorts when the cation at site B moves away from the centre of the cavity.

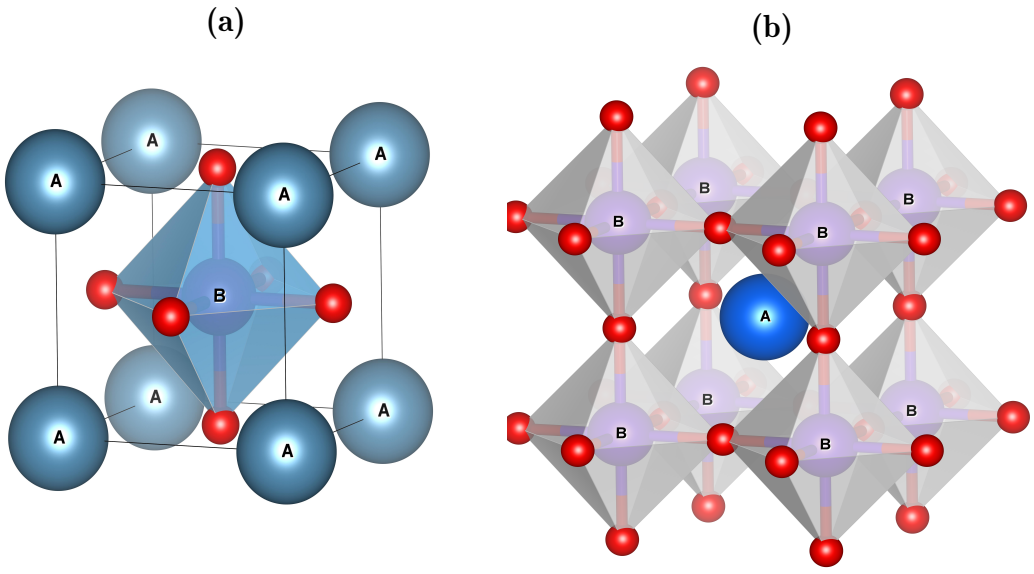

Figure 1.2: Two different ways to represent the cubic ABX_3 perovskite structure. (a): unit cubic cell perovskite ABX_3, (b): BX_6 octahedral in perovskite crystal structure.

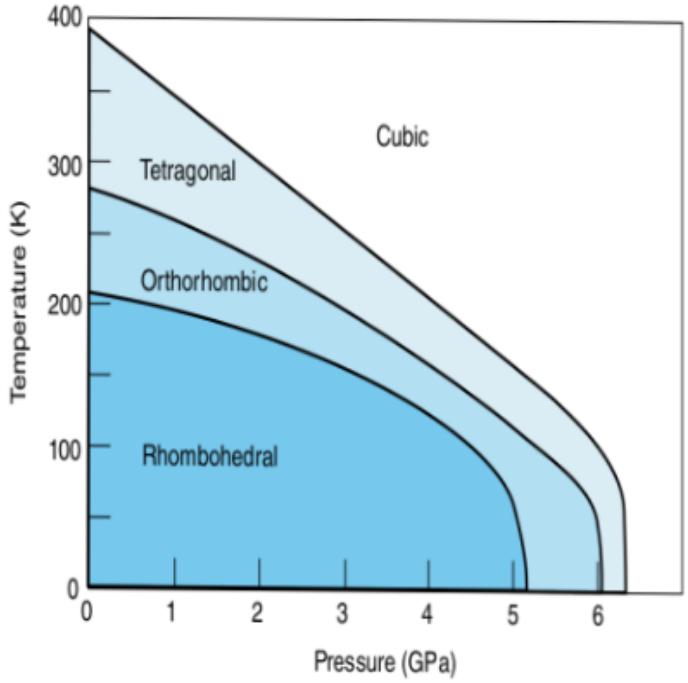

Figure 1.3: Diagram of the temperature and pressure effects on $BaTiO_3$ perovskite structure [1].

1.3 Types of Distortions in Perovskite Structure

1.3.1 Displacement from B Site

The displacement from the B site is measured as the distance in various directions from the centre (0, 0, 0) of the BO_6 octahedra, as illustrated in Figure (1.4). If the cations occupying the B site are notably smaller than the ideal size for a perovskite structure, the lattice undergoes modification. This alteration occurs when the B-site ion moves away from the centre of a BO_6 octahedra. Notably, it is essential to recognize that the degree of displacement in different directions may not be consistent [1, 2, 25].

Identifying the most probable space group for a structure is a reasonably straightforward process. This is because of the distinct positions of the A and B cations, which enable the determination of displacement directions. The displacement of cations can be altered by fluctuations in temperature and pressure, which can cause octahedra distortion.

Figure (1.3) illustrates three distinct space groups of the $BaTiO_3$ perovskite at different temperatures. The displacements of the Ti^{4+} ion in various directions determine the phases at specific temperatures. The structures transform rhombohedral to orthorhombic at 183K, from orthorhombic to tetragonal at around 263K, and from tetragonal to cubic at 393K[46].

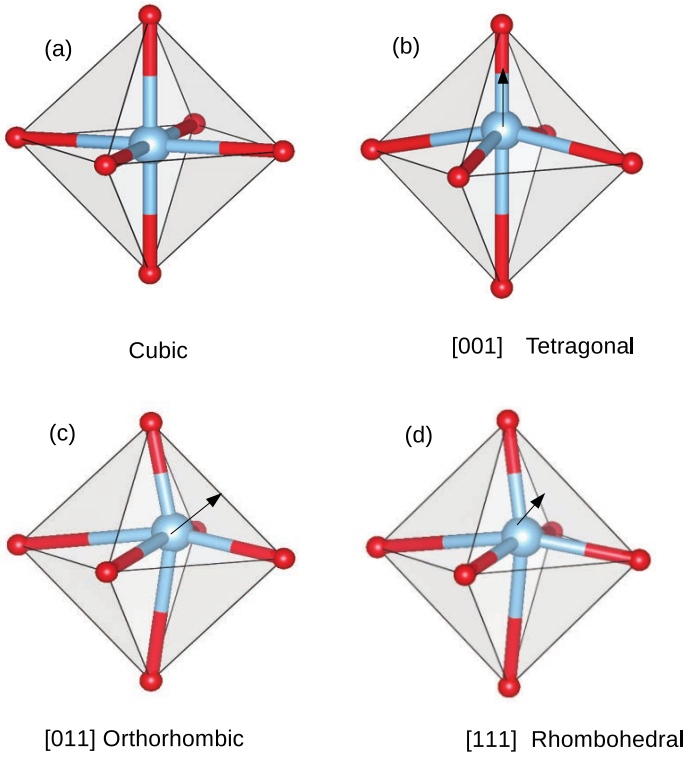

Figure 1.4: B cation displacements along three directions of $BaTiO_3$ [1, 2] .

1.3.2 Octahedral Tilting

At elevated temperatures, the cubic structure is known to exhibit the highest degree of symmetry. However, in perovskite materials, deviations from this ideal structure can be observed due to variations in the size of the A-site ions, which can either be smaller or larger. These deviations are accommodated within the crystal structure through the process of octahedral tilting. Glazer (1972)[47, 48] introduced 23 distinct tilt systems

based on component tilts around axes called "pseudo-cubic," advocating for the concept of octahedral tilting. Table (1.1) presents the tilt systems and corresponding space groups of single and double perovskites. An example is the system labeled $a^0a^0c^+$, which is shown in Figure (1.5). The letters a, b, and c denote rotation angles around the three axes. If the tilt is equal for two axes, the letter is repeated. The superscript zero indicates no tilt along an axis, while the superscript + means a rotation along the z-axis, resulting in two layers of octahedra with identical relative orientations. On the other hand, the superscript − implies a rotation in the opposite direction, as seen in the tilt system $a^0a^0c^-$. The ideal cubic structure is referred to as the no tilt system $a^0a^0a^0$[1].

Table 1.1: Some Glazer's notations of single and double perovskite structures with their respective space groups[49, 50].

TILT	SPACE GROUP	MATERIAL
$a^0a^0a^0$	$Fm\bar{3}m$ ($Pm\bar{3}m$)	Ba_2CaReO_6 ($BiGaO_3$)
$a^0a^0c^-$	I4/m (I4/mcm)	Sr_2CuWO_6 ($SrMoO_3$)
$a^0a^0c^+$	P4/mnc (P4/mbm)	Ba_2PrIrO_6 ($MgSiO_3$)
$a^0b^-b^-$	I2/m(Imma)	Ba_2CaWO_6 ($PbRuO_3$)
$a^+b^-b^-$	$P2_1/n$ (Pnma)	Sr_2ZnWO_6 ($YFeO_3$)

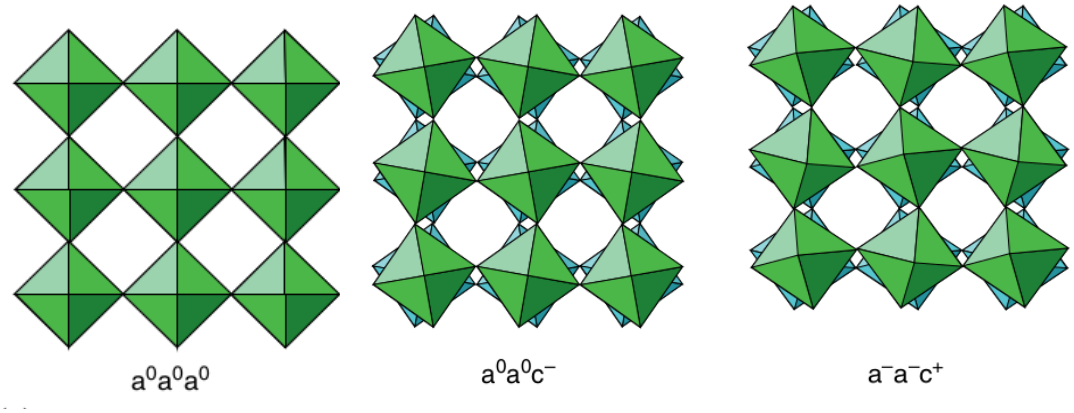

Figure 1.5: Three tilt systems from Glazer's notation structure[1].

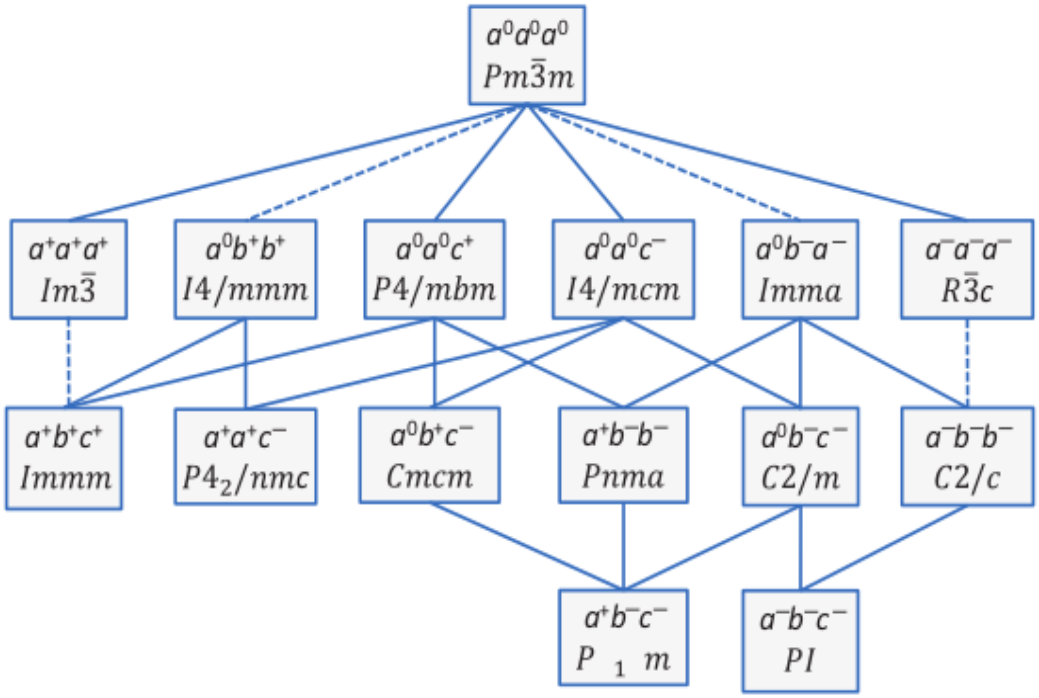

Figure 1.6: 15 Tilt Systems of Double Perovskite[51].

Howard and Stokes [51] expanded upon Glazer's work, presenting 15 tilt systems as depicted in Figure (1.6). However, they opted to exclude the eight additional tilt systems, asserting that each system exhibited a higher level of symmetry than required for the corresponding space group.

1.3.3 Jahn-Teller Effect (JT)

The Jahn-Teller effect, as proposed by Jahn and Teller in 1937, explains that molecules with non-linear structures can undergo geometric distortions, known as Jahn-Teller (JT) distortions, even if they have a degenerate electronic ground state. This phenomenon is exclusive to specific electronic configurations determined by the number of electrons and their respective spin states.

In the molecular orbital theory, specifically Crystal Field Theory, electrostatic interactions explain how electrons are distributed in d or f orbitals of the central atom or ion within various symmetrical environments. Under the influence of the octahedral crystal field (Δ_{CF}), the d-atomic orbitals split into two sets with equal energy levels: t_{2g} and e_g. The t_{2g} shells, situated at a lower energy level, split into three subshells (d_{xy}, d_{xz}, and d_{yz}), while the higher energy e_g shells split into two sub-shells ($d_{x^2-y^2}$ and d_{z^2}). The illustration in Figure 1.7 demonstrates the increase in degeneracy of the d orbitals due to the Jahn-Teller effect and the octahedral crystal field. These distortions effectively eliminate degeneracy by lowering energy and symmetry through the distortion process. In octahedral complexes, when the e_g states, possessing double degeneracy, are partially occupied by one electron, the occupied e_g state undergoes a reduction in energy while the unoccupied state shifts to higher energy levels. JT distortion commonly manifests, causing axial bonds to either lengthen or shorten compared to equatorial bonds.

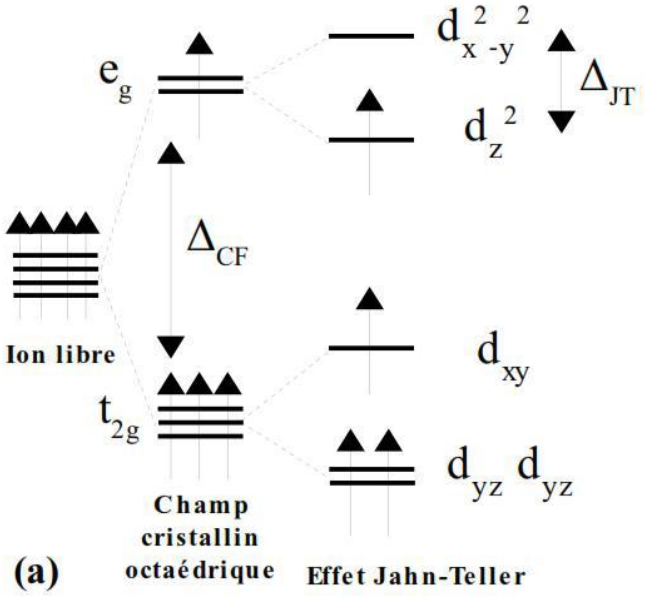

Figure 1.7: The effects of JT distortion and crystal field on the d orbitals of octahedral complexes.

1.4 The double perovskite structure

Perovskite materials are commonly found in various sulfides, halides, and complex oxides[1]. The classification of double perovskite oxides is based on the structure of the single perovskite ABO_3, resulting from substitutions at the cation sites A and B. This leads to two distinct forms: $AA'BO_6$ or $A_2BB'O_6$[52]. Here, A can represent divalent elements of alkaline earth metals such as (Ba^{2+}, Sr^{2+}) or Ca^{2+}, while B signifies trivalent rare earth cations like La^{3+}, Sm^{3+}, Dy^{3+}, Ho^{3+}, Gd^{3+}, Er^{3+}, or Tm^{3+} [34, 53]. The transition pentavalent cation may occupy the B' site, which can be Re^{5+}, Ta^{5+}, Mn^{5+}, Fe^{5+}, or Ru^{5+}.

The same crystallographic form characterizes the perovskite oxide family (refer to Figure 1.2-a). Typically, the A-site cation is occupied by rare alkaline or rare earth elements, while transition metals occupy the B-site cation. A cation is centrally located within the cube at coordinates $(0.5, 0.5, 0.5)$. Furthermore, the B-site cations reside at the corners $(0, 0, 0)$ and are surrounded by six oxygen atoms $(0.5, 0, 0)$, forming an octahedral coordination polyhedron BO_6.

The tolerance factor for the double perovskite structure exhibits similarities to that of the simple perovskite structure, as indicated in equation 1.2.1. In this equation, the ionic radii r_B are distributed between the B and B' sites, averaging $\frac{r_B+r'_B}{2}$.

1.5 RE-double perovskite oxide materials and their properties

1.5.1 Structural and Electronic Properties

The formation of a double perovskite involves substituting half of the BO_6 octahedra in a perovskite structure ABO_3 with suitable $B'O_6$ octahedra. Ion positions in a double perovskite can result in various orderings, such as rock salt, columns, or layers, as depicted in Figure (1.10)[54]. The prevalent arrangement often involves placing two distinct cations, B and B′, in a chessboard-like pattern, commonly known as rock-salt (NaCl) ordering. This arrangement isolates OB_6 and OB'_6 octahedra alternately, resembling a form of zero-dimensional ordering. Additionally, B cations can be arranged in one or two-dimensional orderings, referred to as layered or columnar, respectively.

Rare earth elements (RE) can be located in either A or B positions in the crystal structure of $A_2BB'O_6$. When pentavalent transition metal ions (M^{5+}) are used as the B′ cation and alkaline earth elements are incorporated in the A sites, trivalent rare earth ions (RE^{3+}) can integrate into the B sites. This results in a variety of configurations. The rare earth elements are composed of 15 lanthanides (*La-Lu*), each having either filled or partially filled $4f$ shells. The exception is La, which has an electron configuration of $[Xe]5d^16s^2$. This group also includes yttrium (Y) and scandium (Sc), with electron configurations of $[Kr]4d^1\ 5s^2$ and $[Ar]4s^23d^1$, respectively. Figure (2.3) highlights the rare earth elements in red. Incorporating a lanthanide atom (Ln) at the B position is expected to introduce various electronic and magnetic characteristics.

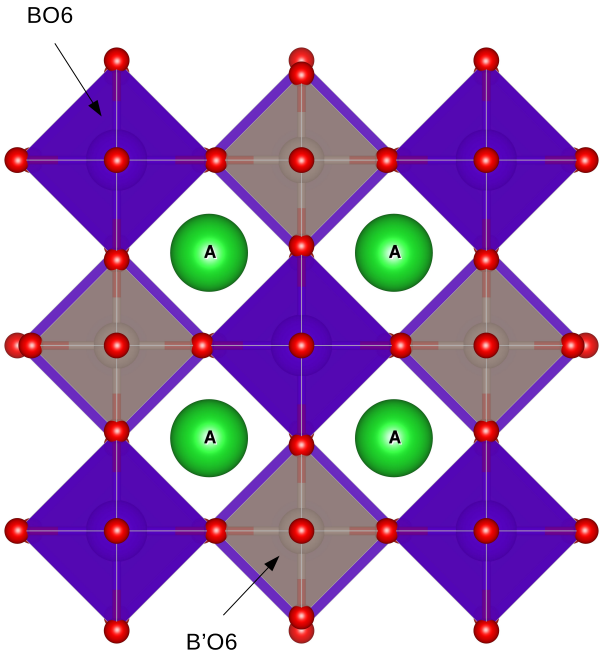

Figure 1.8: Double perovskite structure.

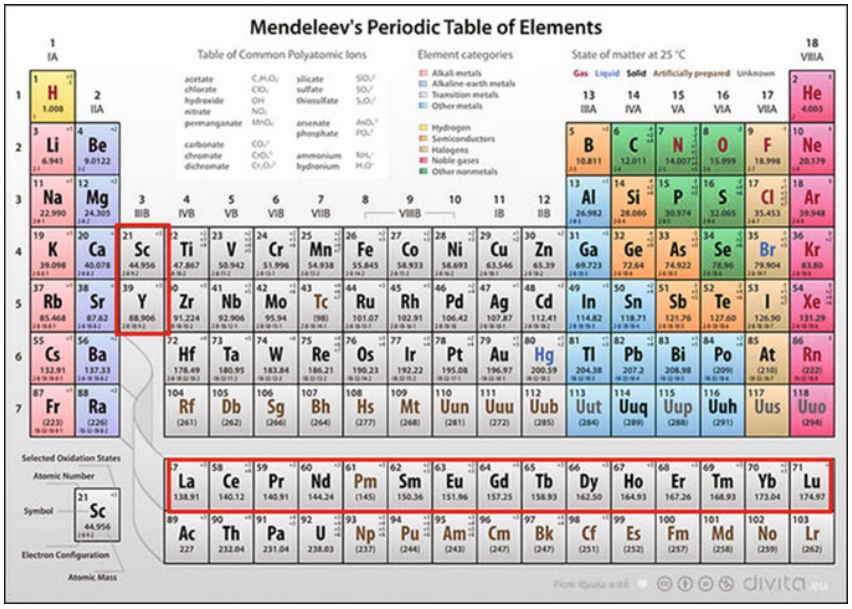

Figure 1.9: The organization of Rare Earth Elements in the Periodic table [55].

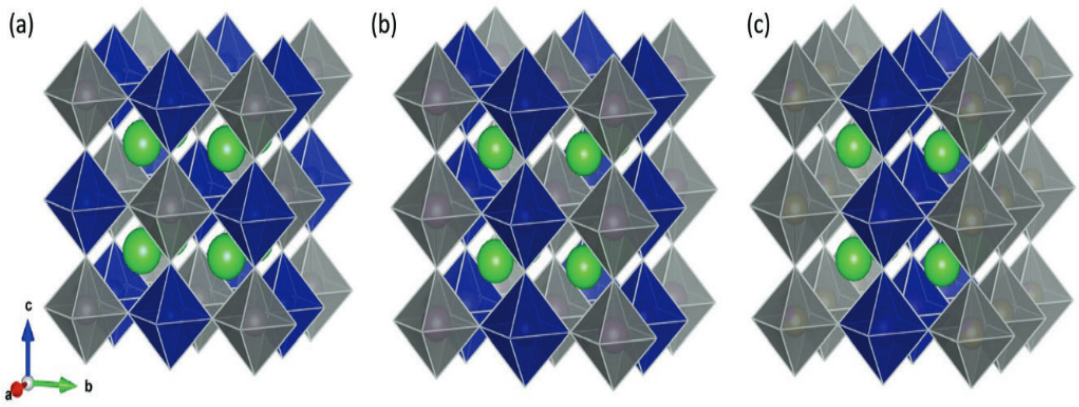

Figure 1.10: Three types of arrangement of B sites in double perovskite: (a) rock salt, (b) columnar, (c) layered.[2].

1.5.2 Magnetic Interactions in Double Perovskites

Double perovskites have been the focus of many investigations due to their favorable magnetic properties. These properties are primarily attributed to the presence of incompletely filled d or f shells at the B′ or B″ sites, which are typically occupied by transition metals and lanthanides. The magnetic characteristics of rare earth materials exhibit significant variability due to the high angular momentum of the f electrons. This leads to diverse states resulting from inter-atomic interactions that depend on the electron count. Generally, double perovskites tend to display antiferromagnetic ordering at low temperatures, which is in contrast to ferromagnetic ordering, owing to interactions between different atoms. At elevated temperatures, these materials commonly exhibit paramagnetic behavior, which may be influenced by temperature-dependent magnetic susceptibility as described by the Curie-Weiss law[56].

Magnetism originates from the rotational motion of electrons and their interactions. It is important to note that most forms of matter exhibit magnetic properties, although to varying degrees. The crucial difference lies in the need for collective interaction among atomic magnetic moments in some materials. In contrast, in others, there is a significantly

stronger interaction, as depicted in Figure 1.11.

Antiferromagnetic behavior manifests when the magnetic moments of nearest neighbors are arranged in opposite directions. Conversely, materials exhibiting **ferromagnetism** feature magnetic moments aligned in parallel within the crystalline structure. The strength of magnetization is notably pronounced when the temperature drops below a specific threshold, known as the FM Curie temperature T_c (Figure 1.11). **Ferrimagnetic** materials showcase a similar arrangement to antiferromagnetic substances (Figure 1.11), although the magnetizations of the sublattices are not entirely nullified. Consequently, a noticeable residual magnetization persists below the Neel temperature.

The interactions with Ru^{5+} ions, which have $4d^3$ electron configuration, are expected to be antiferromagnetic due to the involvement of the half-filled t_{eg} orbitals. Double perovskite materials that have transition metals and lanthanide elements in their B′ and B″ positions exhibit superexchange interactions due to the weak overlapping of RE-M orbitals [25, 57]. The magnetic behavior of A_2LnRuO_6 double perovskites varies depending on the type of Ln element present and the size of the A cation. If the Ln ions are magnetic and have higher Neel temperatures, the compound will exhibit different behavior than if the Ln ions are nonmagnetic. Moreover, the size of the A cation, specifically the transition from Ca to Sr and Ba, affects the type of antiferromagnetic ordering (I, II, or III)[2]. If a double perovskite has only one magnetic cation, its magnetic properties can be compared to those of a simple perovskite. Most Ba_2LnRuO_6 materials, especially those containing Tm, Yb, and Pr, exhibit antiferromagnetic ordering type I. However, if La^{3+} ions are in the B′ position, the antiferromagnetic ordering shows type III due to the presence of nonmagnetic La^{3+} ions at low temperatures[29, 58].

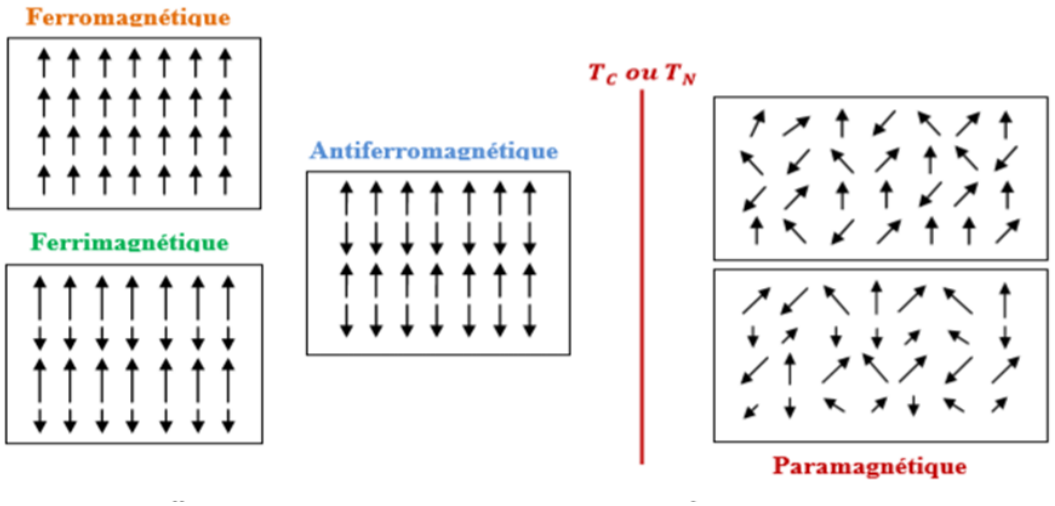

Figure 1.11: (a): antiferromagnetic arrangement, (b): the ferromagnetic arrangement, (c): ferrimagnetic arrangement.

1.5.3 Magneto-Optical Effects

Magneto-optics (MO) is a field that studies the interaction between light and matter in the presence of a magnetic field. Interestingly, magneto-optical effects can occur even without an external magnetic field. The MO Kerr effect (MOKE), which was discovered by physicist S. J. Kerr in 1888, is a significant magneto-optical effect that occurs in the reflection geometry. There are three fundamental configurations of MOKE, namely polar, longitudinal, and transversal geometries. These configurations are determined by the magnetization direction concerning the planes of incidence (M) and reflection. Figure 1.12 illustrates these configurations. In the Polar Magneto-Optical Kerr Effect (P-MOKE) configuration, the magnetization vector and the plane of incidence are perpendicular to the reflecting surface. These results in a rotation of the polarization state, inducing slight ellipticity. The optical phenomenon is characterized by two parameters: the angle of rotation of the polarization plane (θ_k) and the angle quantifying the ellipticity of the reflected light ($\epsilon_k = \arctan(\frac{b}{a})$, where a and b represent the major and minor axes of the resulting ellipse). The dispersion of the optical conductivity tensor is described by the frequency-dependent equation [59]:

$$\sigma_{\alpha\beta}(\omega) = \frac{-ie^2}{m^2\hbar V}\sum_{k}\sum_{mm'}\frac{f(E_{mk}) - f(E_{m'k})}{\omega_{mm'}}\frac{\prod^{\alpha}_{m'm}\prod^{\beta}_{mm'}}{(\omega - \omega_{mm'} + i\gamma)} \tag{1.5.1}$$

The optical dipolar matrix factor, denoted as $\prod^{\alpha}_{m'm}$ and $\prod^{\beta}_{mm'}$, is influenced by the Fermi function $f(E_{mk})$, where $E_{m'k}$ and E_{mk} represent the Kohn-Sham energies at positions k for the two bands m' and m. The difference between these energies, $\hbar\omega_{mm'}$, is equal to $E_{mk} - E_{m'k}$, and the parameter γ represents the lifetime.

The non-diagonal imaginary components of the conductivity tensor characterize magneto-optical absorption. Precisely, in the polar Kerr effect, the magnetization aligns parallel to the z-axis and perpendicular to the sample surface, representing the dielectric tensor as a matrix:

$$\begin{pmatrix} \epsilon_{xx} & \epsilon_{xy} & 0 \\ -\epsilon_{xy} & \epsilon_{xx} & 0 \\ 0 & 0 & \epsilon_{zz} \end{pmatrix} \tag{1.5.2}$$

In the dielectric tensor, the diagonal element is denoted as ϵ_{zz}, while the off-diagonal components are represented by ϵ_{xx} and ϵ_{xy}.

This dielectric tensor plays a crucial role in the formation of the conductivity tensor $\sigma_{\alpha\beta} = \sigma^1_{\alpha\beta} + \sigma^2_{\alpha\beta}$, where the absorptive elements are associated with the absorption of left-handed circularly polarized (LCP) and right-handed circularly polarized (RCP) light [60]. The equations describing the polar Kerr effect (P-MOKE) for linear polarization can be found in the study by Kahn et al. [61]:

$$\phi = \theta_k + i\epsilon_k \tag{1.5.3}$$

Where the polar Kerr rotation and Kerr ellipticity are represented by the integers θ_k and ϵ_k, respectively. This may be stated simply as:

$$\theta_k + i\epsilon_k = \frac{-\sigma_{xy}}{\sigma_{xx}\sqrt{1 + \frac{4i\pi}{\omega}\sigma_{xx}}} \tag{1.5.4}$$

Expressing the off-diagonal and diagonal components of the optical conductivity as σ_{xy} and σ_{xx}, respectively.

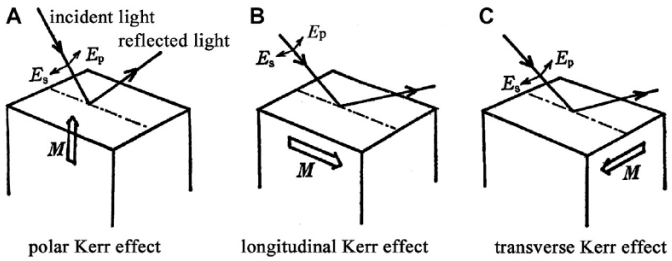

Figure 1.12: The three distinct modes of light reflection on a magnetic surface, known as Magneto-Optical Kerr Effect (MOKE) [62].

1.6 Applications and Utilization of Perovskite Materials

In contemporary electronics, several auspicious materials have emerged as integral components, with perovskite structures playing a pivotal role due to their inherent flexibility and diverse compositions. The following examples highlight the practical applications of double perovskites in various contexts.

1.6.1 Photovoltaic (PV) Devices

In recent years, there has been increasing interest in photovoltaic (PV) systems capable of directly converting sunlight into electrical energy. These systems are recognized as vital solutions to address escalating energy needs, harnessing abundant solar resources [52]. While materials like silicon (Si) and gallium arsenide (GaAs) have been traditional choices for solar cells, halide perovskites, with superior photovoltaic characteristics, have gained attention [63]. However, their vulnerability to environmental conditions impedes practical integration. In contrast, oxide perovskites and their derivatives, known for more excellent stability, find broader use in photovoltaic technologies [52, 64–66].

1.6.2 Spintronic Devices

Conventional electronics rely on utilizing electric charges to process information. Spintronics, an emerging field, integrates electronics and magnetism by leveraging the intrinsic magnetic moment of electrons, known as spin [67]. In spintronics, manipulating both the

charge and spin properties of electrons is crucial for information transfer. Applications include spintronic heads in hard drives and non-volatile devices [68]. Recent focus involves exploring novel half-metallic magnetic materials for spintronics, including ferrimagnetic double perovskites like Sr_2CrReO_6 [69–72].

1.6.3 Solid Oxide Fuel Cells (SOFC)

Fuel cells are a promising solution to address environmental problems, especially global warming caused by greenhouse gas emissions. Ba2LnBO6 double perovskites exhibit potential as anode materials in solid oxide fuel cells, which are designed for stationary use at high temperatures of up to 1000°C. These fuel cells, known as combined heat and power systems, can achieve impressive efficiencies, reaching up to 70% as reported by studies [73, 74].

Chapter 2

METHODOLOGY

- **The concept of (DFT).**
- **Augmented and Linearized Plane Wave Method (FP-LAPW).**
- **WIEN2k code and SPuDs program.**

2.1 The equation of Schrodinger and problem of several particles

In order to comprehend the characteristics of condensed matter, it is necessary to examine a system comprised of electrons and nuclei that interact with one another. According to the principles of quantum mechanics, the behavior of this system is dictated by the many-body Schrodinger equation, which encompasses all of the interactions within the system. This equation was first formulated by E. Schrodinger in 1926 [75, 76], and can be expressed in the following manner:

$$\hat{H}\psi = E\psi \tag{2.1.1}$$

Where the Hamiltonian $\hat{H}$ is a set of variables representing multiple physical interactions within the system, including kinetic energy, potential energy, and interactions with electromagnetic fields.

The Hamiltonian function for a solid with N particles is defined as:

$$\hat{H} = \hat{T}_{el} + \hat{V}_{el} + \hat{T}_Z + \hat{V}_Z + \hat{V}_{el-Z} \tag{2.1.2}$$

- $\hat{T}_{el}$: the electron kinetic energy.
- $\hat{V}_{el}$: the electron-electron interaction.
- $\hat{T}_Z$: the nucleus kinetic energy.
- $\hat{V}_Z$ is the interaction nucleus-nucleus.
- $\hat{V}_{el-Z}$ is the interaction between electrons and nucleus.

Then

$$\hat{H} = -\frac{\hbar^2}{2}\sum_n \frac{\nabla^2_{r_i}}{m_{el}} - \frac{\hbar^2}{2}\sum_n \frac{\nabla^2_{R_n}}{M_n} - \frac{1}{4\pi\epsilon_0}\sum_{n,m}\frac{e^2 Z_n}{\mid \vec{R}_n - \vec{r}_m \mid} + \frac{1}{8\pi\epsilon_0}\sum_{n\neq m}\frac{e^2 Z_n Z_m}{\mid \vec{R}_n - \vec{R}_m \mid} + \frac{1}{8\pi\epsilon_0}\sum_{n\neq m}\frac{e^2}{\mid \vec{r}_n - \vec{r}_m \mid} \tag{2.1.3}$$

The Hamiltonian operator, which accounts for the motion and interactions of all atoms within a solid, presents a challenge when applied to systems with multiple bodies. To

address this issue, the equation can be simplified by breaking it down into a set of individual equations that describe the motion of each particle. This process necessitates the development of approximations. The first simplification is achieved by adopting the Born-Oppenheimer approximation [77].

2.1.1 Born-Oppenheimer approximation (1927)

The resolution of the Schrodinger equation in crystal systems is a complex task due to the multitude of interactions depicted in equation (3.3.1). M. Born and J.R. Oppenheimer[77] proposed that nuclei can be considered fixed, while the electrons are much lighter than the nuclei. As a result, the momentum of the nuclei becomes slower. This assumption results in the nuclei having zero kinetic energy ($T_Z = 0$)[78]. Leading to a separation of the electronic and nuclear wave functions, this allows for the independent calculation of the levels of electronic energy and wave functions of a molecule from the nuclei.

The Hamiltonian is reduced as follows:

$$\hat{H} = \hat{T}_{el} + \hat{V}_{el-el} + \hat{V}_{ext} \tag{2.1.4}$$

The wave function of a crystal is influenced by both electrons and nuclei, and can be divided into two components based on their respective contributions (Ψ_{el}, Φ_Z). The kinetic energy of the electron gas in a solid can be described as the energy resulting from the interaction between two electrons, which creates a potential energy represented by $\hat{V}_{el-el}$. The external potential of positively charged nuclei is denoted by $\hat{V}_{ext}$.

$$\Psi(\vec{r}_i; .....; \vec{R}^0_\alpha) = \Psi_{el}(\vec{r}_i; ....; \vec{R}^0_\alpha)\Phi_Z(\vec{R}^0_\alpha) \tag{2.1.5}$$

The wave function of electrons, represented by Ψ_{el}, depends on the positions of the electrons ($\vec{r}_i$, where $i = 1...n$) and the fixed nuclei ($\vec{R}^0_\alpha$). The nuclear wave function is denoted as Φ_Z.

In order to obtain a solution for the Schrodinger equation, a set of fixed nucleus locations is utilized as parameters. The resolution of the equation requires solving a set of equations:

$$\hat{H}_e\psi_{el} = E_{el}\psi_{el} \tag{2.1.6}$$

Then

$$[-i\frac{\hbar^2}{2}\sum_n \frac{\nabla^2_{r_i}}{m_{el}} + \frac{1}{8\pi\epsilon_0}\sum_{n\neq m}\frac{e^2}{\mid \vec{r}_n - \vec{r}_m \mid} - \frac{1}{4\pi\epsilon_0}\sum_{n,m}\frac{e^2 Z_n}{\mid \vec{R}_n - \vec{r}_m \mid}]\psi_{el} = E_{el}\psi_{el} \tag{2.1.7}$$

E_{el} represents the energy of electrons that move in the field created by the fixed nucleus ($E_{el}(R^0_\alpha)$).

It is important to acknowledge that the motion of nuclei is governed by a distinct wave function, denoted as $\Phi_Z(\vec{R}_{1,.....})$. Subsequently, we undertake the task of resolving the given equation:

$$\hat{H}_Z\Phi_Z = E\Phi_Z \tag{2.1.8}$$

$$\hat{H}_Z\Phi_Z = \sum_\alpha(\frac{-\hbar^2\Delta^2_\alpha}{2M_\alpha} + \hat{V}_Z + E_e(..,\vec{R}_1,..))\Phi_Z = E\Phi_Z \tag{2.1.9}$$

The nuclear wave function Φ_Z describes the average value of electron motion.

The Born-Oppenheimer approximation exhibits several notable deficiencies, a few of which are outlined below:

► The Born-Oppenheimer approximation may prove inadequate in cases where electronic and vibrational motions are closely intertwined, despite its assumption to the contrary. This can result in non-adiabatic consequences.

► Due to the potential variability of nuclear coordinates, it cannot be assumed that the electronic wave function will remain constant, which leads to electronic relaxation. This phenomenon is not accounted for by the Born-Oppenheimer approximation.

► The Born-Oppenheimer assumption becomes unreliable when subjected to high pressure or temperatures because it assumes that the nuclei are stationary at their equilibrium positions. However, at such conditions, the nuclei can experience significant displacement.

►The Born-Oppenheimer methodology relies on the concept of isolating the ground state of the electron from its excited states. However, this hypothesis proves inadequate when illustrating electronic states that are significantly elevated.

At this level, there exist multiple approaches to address equation 2.1.5,the initial ones

being the Hartree and Hartree-Fock methods, which rely on the assumption of free electrons [79, 80].

2.1.2 Hartree and Hartree-Fock approximation (1928-1930)

The Hartree approach, based on the independent electron approximation [81, 82], employs the Jellium model to simplify the problem of solving a system of single-particle differential equations. This model assumes that electrons in a material behave like a homogeneous electron gas, thereby simplifying the problem. The Hartree approximation neglects the interactions between electrons and spin states, but it accounts for the mean field potential. The overall wave function is obtained by separating it into the wave functions of individual particles $\psi^i(\vec{r})$:

$$\psi^H(\vec{r}) = \psi^1(\vec{r}_1).\psi^2(\vec{r}_2).\psi^3(\vec{r}_3)....\psi^N(\vec{r}_N) \tag{2.1.10}$$

The equation (2.1.10) mentioned above lacks asymmetry when two electrons are permuted, indicating that these electrons are classified as fermions. As such, the electron spin and Pauli exclusion principle are not disregarded, necessitating the alteration of ψ's sign upon the permutation of two electrons. The total wave function must therefore be asymmetric and expressed in the following format:

$$\psi^H(\vec{r_1}, \vec{r}_2, ..., \vec{r}_N) = -\psi^H(\vec{r_1}, \vec{r}_2, ..., \vec{r}_N) \tag{2.1.11}$$

Hence. Fock suggested adopting a linear combination of independent electron wave functions in a solitary Slater determinant configuration to express the wave function of a system with N electrons [83]. This configuration is expressed in the following form [84]:

$$\psi^{HF}(\vec{r_1}, \vec{r_2}, ...\vec{r_n}) = \frac{1}{\sqrt{n!}} \begin{vmatrix} \psi^1(\vec{r_1}) & \psi^2(\vec{r_1}) & ... & \psi^N(\vec{r_1}) \\ \psi^1(\vec{r_2}) & \psi^2(\vec{r_2}) & ... & \psi^N(\vec{r_2}) \\ \vdots & \vdots & ... & \vdots \\ \psi^1(\vec{r_n}) & \psi^2(\vec{r_n}) & ... & \psi^N(\vec{r_n}) \end{vmatrix} \tag{2.1.12}$$

Where $\psi^{HF}(\vec{r_i})$: is the one-electron wave function that depends on the local coordination of the electron spin and vector $\vec{r_i}$.

The normalization factor, denoted as $\frac{1}{\sqrt{n!}}$, is used in the context of the determinant of Slater, which exhibits anti-symmetry. Pierre Hohenberg and Walter Kohn's seminal paper on the symmetry principle and exchange effects yielded highly satisfactory results. However, the Hartree-Fock wave function fails to account for the electronic correlation term of the system.

By utilizing the variational method to minimize the Hamiltonian operator, the average electronic energy E_e can be determined:

$$\langle H \rangle = \frac{\langle \psi^{HF} | H | \psi^{HF} \rangle}{\langle \psi^{HF} | \psi^{HF} \rangle} \tag{2.1.13}$$

The field of calculus of variations demonstrates that the wave function $\psi^{HF}(\vec{r})$ for each system must minimize the average energy $\langle H \rangle$. The wave functions are obtained as solutions of a second-order differential equation, which is analogous to Schrödinger's equation for a single particle. In order to account for electronic correlations, several techniques have been developed that surpass the Hartree-Fock method. These techniques rely on density functional theory (DFT) [85–87].

Density functional theory (DFT)

The Density Functional Theory (DFT) is a reformulation of the N-body quantum problem that focuses solely on the electron density. The original idea of this theory was developed by Thomas and Fermi in 1927[88, 89]. In their initial work, Thomas and Fermi neglected electron-electron interactions and treated the system as a homogeneous gas, with the kinetic energy being a function of the local density [90]. They did not account for the effects of exchange and correlation between electrons, but Dirac addressed this deficiency in 1930 [91] when he introduced the local exchange approximation [91].

This concept depends on the electronic density and replaces the Schrodinger equation with a set of self-consistent equations. Upon solving these equations, the energy and electron density of the entire system can be obtained:

$$\hat{H} = \sum_{i=1}^{N} \left[-\frac{\hbar^2}{2m} \nabla_i^2 + V_{ex}(\mathbf{r}_i) \right] + \frac{1}{2} \sum i = 1^N \sum_{j=1, j \neq i}^{N} \frac{e^2}{|\mathbf{r}_i - \mathbf{r}_j|} \tag{2.1.14}$$

The Hamiltonian consists of the kinetic energy of the electron and the Coulomb interactions. However, the computational complexity of evaluating this equation for systems with a large number of electrons is a persistent challenge. Density Functional Theory (DFT) has emerged as a valuable tool to address this issue.

In this context, the electronic density ($\rho(\mathbf{r})$) serves as the primary variable for describing the energy of the system. The electronic density functional $E[\rho]$ is used to represent the energy of the system, while the exchange-correlation functional $E_{xc}[\rho]$ relates the electronic density to the external potential V_{ext} and the electron-electron interactions. Consequently, the energy of the system can be expressed as a function of these variables.

$$E_{tot} = T_s[\rho] + \int V_{ext}(\mathbf{r})\rho(\mathbf{r})d\mathbf{r} + E_{xc}[\rho] \tag{2.1.15}$$

The functional $T_s[\rho]$ represents the density of kinetic energy for the non-interacting electron gas. By minimizing the total energy with respect to the electronic density, one can determine both the electronic density and the V_{ext}.

The importance of Density Functional Theory (DFT) lies in its relative simplicity compared to Schrodinger's equation. By utilizing the equations developed by Hohenberg[92], Kohn, and Sham[93, 94], it becomes possible to solve the self-consistent equations.

2.2 Hohenberg-Kohn theorems

According to the Hohenberg-Kohn theorems. [92], the electron density is the sole determinant of a system's electronic properties.

1. In the context of an electron gas, the HK theorem demonstrates that the system's fundamental state and associated charge density are governed by the external potential acting on these particles. Therefore, the energy functional $E[\rho]$ is expressed using the formula for $\rho(r)$.

$$E[\rho] = \langle \phi | H | \phi \rangle = G[\rho] + \int V_{ex}(r_i)\rho(dr) \tag{2.2.1}$$

The HK universal functional is $G[\rho]$[92, 95], This combines all the variables that are independent of the external potential V_{ex}, including the XC interaction and electron kinetic energy:

$$G[\rho] = \langle\psi|T_e + U_{e-e}|\psi\rangle \tag{2.2.2}$$

2. The minimal functional of the total energy $E[\rho(r)]$, for any multi-particle system, which corresponds to the ground state density[92] is described as:

$$\frac{\delta E[\rho(r)]}{\delta\rho(r)} = 0 \tag{2.2.3}$$

The second theorem, which utilizes the variational principle, aims to calculate the density of the ground state for a given external potential V_{ex}. The objective is to determine the two unknown variables in equation (2.2.2), namely $T_e[\rho]$ and $U_{e-e}[\rho]$. However, the Hohenberg-Kohn theorem does not provide any information regarding the $G[\rho]$ term. Therefore, it becomes necessary to employ approximations that are consistent with the Kohn and Sham[96] equations.

2.3 Kohn-Sham equations

The concept of the Kohn-Sham (KS) method is based on representing a system of N interacting fermions in an external potential V_{ext} as a fictitious system of N non-interacting electrons that move in an effective potential V_{eff} [96, 97]. This approach establishes a direct relationship between the electron density and the energy of the ground state of the non-interacting fermions in the effective potential V_{eff}. Consequently, the electron density functional can be expressed using the following equation [98]:

$$G[\rho(r)] = T[\rho(r)] + U_H[\rho(r)] + V_{xc}[\rho(r)] + V_{ex}[\rho(r)] \tag{2.3.1}$$

Where, T is the kinetic energy of the fictitious system:

- $T[\rho(r)]=\sum_i^N \int \psi_i^*(r)\frac{-\hbar^2\nabla^2}{2m}\ \psi_i(r)$.
- U_H is the Hartree potential: $U_H\ [\rho(r)]=\frac{1}{2}\int \frac{\rho'(r)}{r-r'}dr$
- V_{xc} is the term that includes the XC effects: $V_{xc}[\rho(r)] = \frac{\delta E_{xc}[\rho(r)]}{\delta\rho(r)}$.

▶ V_{ex} is the external potential.

The solution to the Schrodinger equations is obtained through a set of three separate equations, commonly known as the Kohn-Sham equations [93]:

1. The first equation represents the effective potential:

$$\rho(r) \rightarrow V_{eff}(r) = U_H + V_{xc}(r) + V_{ex}(r) \tag{2.3.2}$$

2. the second equation is the Kohn-Sham approach's Schrodinger equation H^{KS} has the following form:

$$H^{KS}\psi_{i(r)} = (\frac{-\nabla_i^2}{2} + V_{eff})\psi_i(r) = \varepsilon_i^{KS}\psi_i(r) \tag{2.3.3}$$

Where the Kohn-Sham Hamiltonian, the energy eigenvalues ε_i^{KS} $(i = 1, 2, ...N)$, and $\psi_i(r)$ are the specific wave functions of an electron.

3. The third one defines the electronic density:

$$\psi_i(r) \rightarrow \rho(r) = \sum_{i=1}^{N} |\psi_i(r)|^2 \tag{2.3.4}$$

2.4 equations resolution

The resolution of the KS equations involves finding the eigenvalues and eigenfunctions that correspond to the system's fundamental state. This requires solving self consistently [96]. The solution process comprises several stages, starting with an initial assumption for the electronic density. The potential $V_{eff}(r)$ is then calculated using equation (2.3.2) in order to solve equation (2.3.3) for $\psi_i(r)$. This solution provides a new density for equation (2.3.4) in order to update the potential. The updated potential is then used to solve the KS equations again, and the process is repeated until convergence is achieved. At convergence, the electron density and potential reach a self-consistent solution, as depicted in the diagram below (2.1).

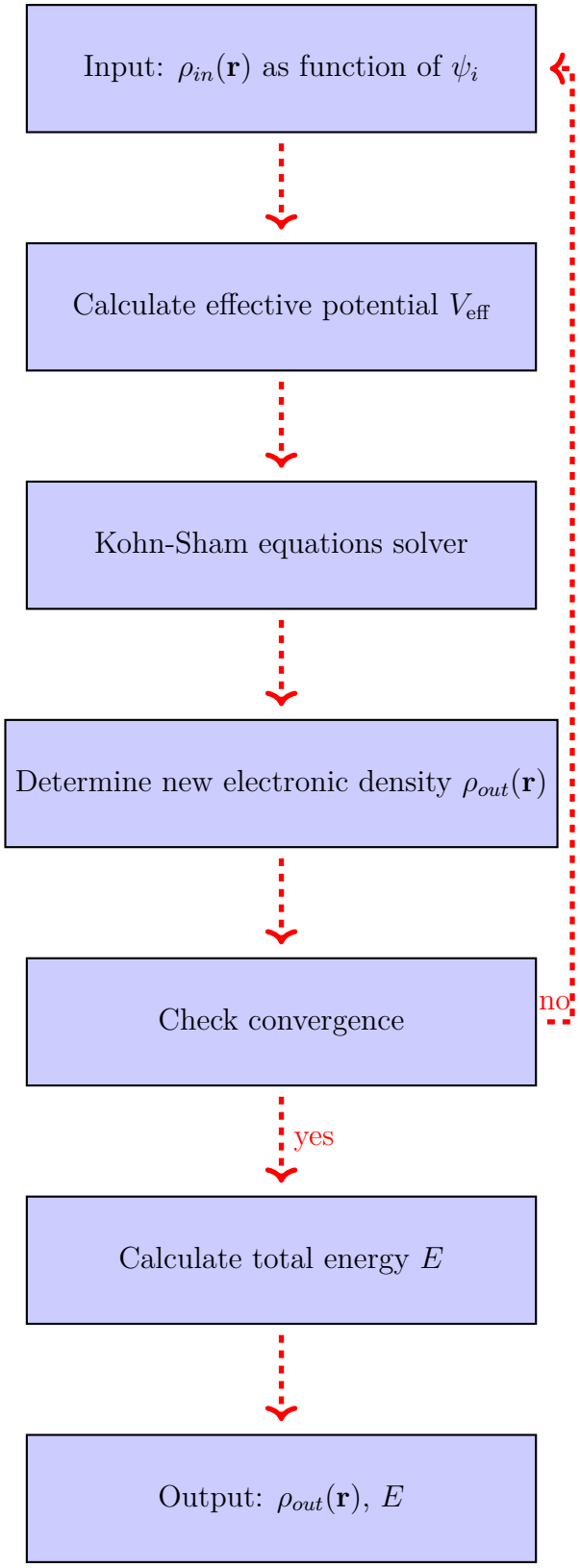

Figure 2.1: The auto-coherent Kohn-Sham diagram.

2.5 The exchange correlation functional

Within the framework of Density Functional Theory (DFT), the exchange-correlation functional plays a crucial role in calculating the total energy. This functional can be divided into two components, namely the exchange functional, which accounts for the electron-electron interaction, and the correlation functional, which describes the correlation between electrons. Despite its significance, the precise form of the exchange-correlation functional, denoted as V_{xc}, remains uncertain. To approximate this functional, various exchange-correlation functionals, such as the local density approximation (LDA), have been proposed. The V_{xc} functional is defined as a function of the electron density, which is based on the concept of Bloch, who postulated that the exchange-correlation could be expressed using the Fermi statistics of a uniform electron gas. [99–105]

2.6 The local density approximation (LDA)

Kohn and Sham formulated the local density approximation (LDA)[96, 103] by postulating that the exchange-correlation energy (E_{xc}) for a given density can be determined by dividing the matter into small volumes with uniform density. Each volume contributes an amount to the overall E_{xc} that is equivalent to that of a volume of the same size containing a homogeneous electron gas with the same total density as the material of origin. As a result, the exchange-correlation energy can be expressed as:

$$E_{xc}^{LDA}[\rho(r)] = \int \rho(r)\epsilon_{xc}[\rho(r)]dr^3 \tag{2.6.1}$$

$\epsilon_{xc}[\rho(r)]$ in a system of homogeneous electrons with the density $\rho(r)$, is the exchange correlation energy contribution made by each electron [106]. Additionally, ϵ_{xc} could potentially be divided into two terms: ϵ_x and ϵ_c, which stand for exchange and correlation, respectively:

$$\epsilon_{xc}^{LDA}[\rho(r)] = \epsilon_x[\rho(r)] + \epsilon_c[\rho(r)] \tag{2.6.2}$$

The correlation term could be writing as: $\epsilon_x[\rho(r)] = -\frac{3}{4\pi r_s}(\frac{9\pi}{4})^{\frac{1}{3}}$: it is coming out of the Dirac exchange functional[91].

The equation (2.6.1) can be readily utilized for the analysis of spin-polarized magnetic systems. Zunger[107] proposed the Local Spin Density Approximation (LSDA) that accounts for both electron density and spin density by estimating them as functions of the exchange-correlation energy at all points in space $\vec{r}$. The spin density, as expressed in the subsequent equation, characterizes the distribution of magnetic moments of electrons in space.

$$E_{xc}^{LSDA}[\rho(r)] = \int (\rho_{\uparrow}(r) + \rho_{\downarrow}(r))\epsilon_{xc}[\rho_{\uparrow}(r), \rho_{\downarrow}(r)]dr^3 \tag{2.6.3}$$

To address the limitations of the local density approximation (LDA), advanced density functionals have been developed that incorporate additional information beyond the local electron density. Perdew (1986) aptly references the Generalized Gradient Theory (GGA) [108], which integrates information on the gradient of the electron density to enhance accuracy.

2.7 Generalized gradients approximation(GGA)

The generalized gradient approximation (GGA) is a method that improves upon the local density approximation (LDA) for calculating the exchange-correlation energy in electronic structure calculations. This is achieved by taking into account both the electron density and its gradient, denoted as $\nabla\rho(r)$[108]. The GGA approximation can be expressed mathematically as follows:

$$E_{xc}^{GGAs}[\rho(r)] = \int \rho(r)\epsilon_{xc}[\rho(r)|\nabla\rho(r)|]dr^3 \tag{2.7.1}$$

Where $\epsilon_{xc}[\rho(r)|\nabla\rho(r)|]$[109] represents the exchange-correlation energy per electron in a system of mutually interacted electrons of inhomogeneous density. In other hand, the GGAs[110] approximation with spin polarization could be described in the following equation:

$$E_{xc}^{GGA}[\rho(r)] = \int (\rho_{\uparrow}(r) + \rho_{\downarrow}(r))\epsilon_{xc}[\rho_{\uparrow}(r), \rho_{\downarrow}(r), \nabla_{\uparrow}\rho(r)_{\uparrow}, \nabla_{\downarrow}\rho(r)_{\downarrow}]dr^3 \tag{2.7.2}$$

The GGAs exhibited superior performance compared to LSDA. It is widely acknowledged

that LSDA underestimates the equilibrium lattice constant by 1-3% [110]. In 1986, Perdew et al. developed an estimation technique, known as PW86[111], to address the correlation term. This approach has been documented in literature, including PW91[112] by Perdew and Wang, and PBE[113], a reformulation of PW91 by Perdew, Burke, and Enzerhof[114–116]. These approximations are widely recognized in the field.

2.8 DFT+U approximation

In systems with highly localized d or f shells, the main idea of DFT+U is to introduce a significant intra-site effective Coulomb repulsion among localized electrons. The reason for this is that the LDA and GGA methods are inadequate for predicting the properties of excited states. These methods underestimate the gap between semiconductors and insulators, which is also known as the Hubbard term, U. We utilized a modified version of the DFT+U approach developed by Dudarev et al.[117], which involves combining the DFT approach (LDA or GGA with spin polarization) with a Hubbard Hamiltonian. The Hamiltonian is expressed in a Hamiltonian of a particular form
citesouidietude,anisimov1991band:

$$H = \frac{U}{2} \sum_{m,m',\sigma} \hat{n}_{m\sigma}\hat{n}_{m',\sigma} + \frac{U-J}{2} \sum_{m,m',\sigma} \hat{n}_{m\sigma}\hat{n}_{m',\sigma} \tag{2.8.1}$$

At a particular point, $n_{m\sigma}$ is the operator that determines the number of electrons occupying a state with magnetic quantum number m (m') and spin σ (σ').

The spherically averaged Hubbard parameter, denoted as U [118], measures the energy required to add an additional electron to a specific site. The Stoner exchange parameter can be approximated by J. Meanwhile, U and J are used to describe the intra-site Coulomb repulsion.

Moreover, the role of U and J is not individual, but instead they contribute through their disparity($U_{eff} = U - J$). The value of the U coefficient is typically derived from literature computations or experimental work[117, 119]. In our work, we used this method.

2.9 Spin-orbit coupling (SOC)

The inclusion of the spin-orbit (SOC) term, which is often disregarded in the relativistic approximation. This phenomenon arises from the interplay between the spin of an electron and the magnetic field produced by the electron's orbital motion within a fluctuating electrostatic potential surrounding the nucleus. The SOC plays a crucial role in accurately determining the magneto-optical properties of materials that consist of heavy elements or exhibit magnetic behavior[120].

Augmented and Linearized Plane Wave Method (FP-L/APW)

2.10 The method (APW)

There are several computational codes that are used to solve the band structure problem using DFT. Researchers have developed methods that utilize theoretical concepts known as first-principle methods, including FP-LAPW[121], LMTO[122], PP-PW[123], FPLO[124], and KKR [125]. These methods are commonly employed in density functional theory (DFT) research.

The augmented plane wave (APW)[126] approach, created by Slater in 1937[127–129], was improved upon by the LAPW method, which integrates the Full potential (FP). This method operates on the principle that the potential and wave functions near the atomic nucleus take the form of a "Muffin-Tin" (MT) within a sphere of radius r_α. They exhibit spherical symmetry within this region. Two areas consist of the division of the unit cell: the MT region, and in contrast to the potential and wave functions in the interstitial area among atoms, which may be roughly described as flat, the potential in the MT area exhibits spherical symmetry[130]. Therefore, the wave functions of the crystal are computed using with various basis. Additionally, the Schrodinger equation has radial solutions inside the MT spheres, while outside the sphere region, the solutions are plane waves, as illustrated in the figure bellow (2.2).

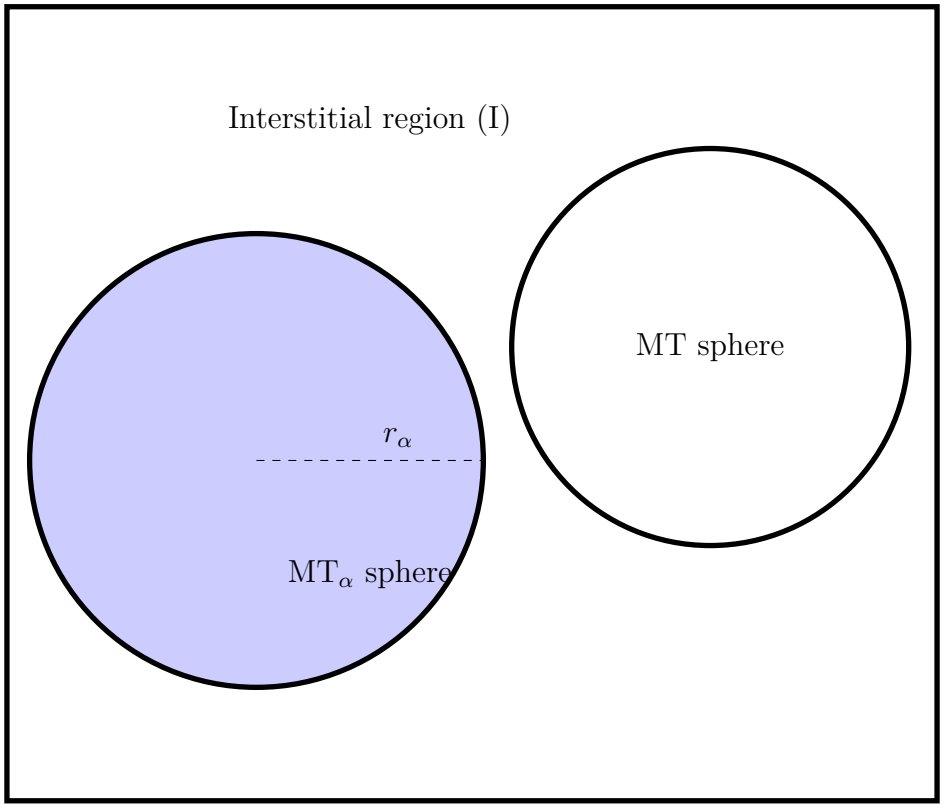

Figure 2.2: Muffin-Tin potential

The crystal potential is constant in the space between the cores. When the wave function $\phi(r)$ is written in the form of[131]:

$$\phi(\vec{r}) = \begin{cases} \frac{1}{\Omega^{\frac{1}{2}}} \sum_{\vec{G}} C_{\vec{G}} e^{i(\vec{G}+\vec{k})\vec{r}}, \ \vec{r} \in I \\ \sum_{lm} A_{lm} U_l(r, E) Y_{lm}(r), \ \vec{r} \in MT_\alpha \end{cases} \tag{2.10.1}$$

The MT_α represents the MT sphere α, $\vec{k}$ is the Bloch vector, r_α is the radius of the vector position of the MT sphere. The symbols $\vec{G}$ and Ω respectively represent the reciprocal lattice vector and the primitive volume. $C_{\vec{G}}$ and A_{lm} are the coefficients in the spherical harmonics Y_{lm}. The variable r represents the position in polar coordinates within the sphere.

The Schrodinger equation solution $U_l(r, E)$ for radial part is given as:

$$\left\{ -\frac{d^2}{d^2 r} + \frac{l + (l+1)}{r^2} + V_r - E_l \right\} \ rU_l(r) = 0 \tag{2.10.2}$$

Where $V(r)$ represents the Muffin-Tin (MT) potential and E_l represents the linear energy.

The radial functions U_l are orthogonal in every proper state of the core. When the MT sphere reaches its boundaries, this orthogonality vanishes [132], as shown by the following equation:

$$(E_2 - E_1)rU_1U_2 = U_2\frac{d^2U_1}{d^2r} - U_1\frac{d^2U_2}{d^2r} \tag{2.10.3}$$

U_1 and U_2 are the radial solutions corresponding the energies E_1, E_2[131].

To ensure the functionality of the surface of the MT sphere, the coefficients A_{lm} can be generated using the existing C_G plane wave coefficients found in the interstitial region:

$$A_{lm} = \frac{4\pi i^l}{\Omega^{\frac{1}{2}}U_1(\vec{R}_\alpha)}\sum_{\vec{G}} C_{\vec{G}}J_l(|\vec{K}+\vec{g}|\vec{R}_\alpha)Y^*_{lm}(\vec{K}+\vec{G}) \tag{2.10.4}$$

J_l represents the Bessel function of order l [133].

The computation of A_{lm} coefficients is reliant on the imposition of continuity on $U_l(r, E)$ and the corresponding plane wave on the muffin-tin sphere. Slater justified the specific choice of these functions by noting that plane waves provide solutions to the Schrodinger equation if the potential is constant, while radial functions are solutions in a spherical potential when E_l is equal to an eigenvalue. This approximation is highly accurate for materials with cubic face-centered structures, but becomes less satisfactory as the symmetry of the material decreases.

The main problem caused by this method is the discontinuity of the function $\Psi(\vec{r}, E)$ at the surface of the MT sphere. In order to ensure continuity at this boundary, the coefficients A_{ml} must be expanded in terms of the coefficients C_G. In this expansion, if the radial part $U_l(r, E)$ becomes zero for a certain value of E, there will be no continuity. To overcome this, several modifications of the method have been proposed by Koelling and Andersen[134, 135].

2.11 FP-LAPW method

The full potential linearized augmented plane-wave (FP-LAPW) variational expansion approach is used to solve the DFT equations [121, 136]. This method utilizes basis

functions that are formed by linearly combining radial functions $U_l(r)Y_{lm}(r)$ and their energy derivatives within the MT spheres[137].

The LAPW method employs plane waves as functions solely within the interstitial region, similar to the APW method[134, 135]. However, within the spheres, the functions are augmented by linear plane waves that offer greater variational freedom. The radial function U_l can be described in terms of its derivative $\dot{U}_l = \frac{dU_l(r,E)}{dE}|_{E=E_l}$, where E_l is a fixed value:

$$\left\{-\frac{d^2}{d^2r} + \frac{l+(l+1)}{r^2} + V_r - E_l\right\} r\dot{U}_l(r) = rU_l(r) \tag{2.11.1}$$

The values and derivatives of plane waves on the boundaries of the sphere in the context of the non-relativistic case correspond to the functions. These plane waves are enhanced and become the LAPW basis functions, also known as LAPWs[131]. Consequently, the wave functions are shown in terms of:

$$\phi(\vec{r}) = \begin{cases} \frac{1}{\Omega^{\frac{1}{2}}} \sum_{\vec{G}} C_{\vec{G}} e^{i(\vec{G}+\vec{k})\vec{r}}, \ \vec{r} \in I \\ \sum_{lm}(A_{lm}U_l(r,E_l) + B_{lm}\dot{U}_l(r,E_0))Y_{lm}(r), \ \vec{r} \in MT_\alpha \end{cases} \tag{2.11.2}$$

The B_{lm} coefficients represent the derivative of energy and are similar to the A_{lm} coefficients. The coefficients A_{lm} and B_{lm} are determined in such a way that each basis function and its derivative are continuous at the interface between Muffin-Tin spheres and the interstitial region.

$$U_l(r,E) = U_l(r,E) + (E-E_l)\dot{U}_l(r,E_l) + O((E-E_l)^2) \tag{2.11.3}$$

The error introduced in the calculation of the wave function and band energy is of the order of $O((E-E_l)^2$ and $(E-E_l)^4$ [135], respectively. However, despite this order of error, the linearly augmented plane waves (LAPW) form a good basis that allows for the treatment of all valence bands within a large energy range using a single value of E_l. In cases where this is not possible, the energy window can generally be divided into two parts, which is a significant simplification compared to the APW method. In general, if the U_l is null at the surface of the sphere then, its derivative $\dot{U}_l \neq 0$, then the problem

of continuity of the wave function at the MT sphere surface does not arise in the LAPW method.

2.12 Modification of FP-LAPW

The primary challenge confronting the LAPW technique pertains to the inadequacy of a single set of E_l to effectively account for all valence bands, particularly in materials that contain 4f orbitals [138, 139]. The situation is commonly referred to as the semi-core state, which indicates an intermediate state that exists between the valence and core states. To address this issue, the initial approach involved dividing the energy levels into multiple windows or developing local orbitals.

2.12.1 Multiple energy windows

In this window-based treatment, a distinction is made between the valence state and the semi-core state, where a set of El is chosen for each window to handle the corresponding states. This entails performing two independent LAPW calculations, albeit with the same potential, as shown in figure bellow (2.3)[140, 141]:

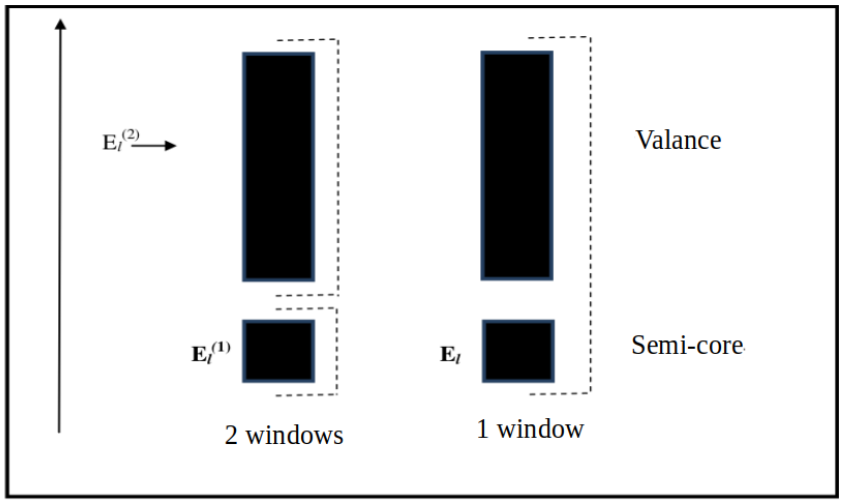

Figure 2.3: exemple of multiple energy windows.

2.12.2 Locales orbitals

The LAPW method was devised as a means of obviating the necessity for multiple energy windows by modifying the local orbitals of its basis. The objective of this technique is to address all energy bands using a single energy window, which can be achieved by designating the semi-core state. Various suggestions have been put forward by Takeda et al. [142–144]. Singh [145] has recently proposed a method that involves combining two radial functions with different energies in a linear manner and deriving one of these functions:

$$\phi_{lo}(\vec{r}) = \sum_{lm}(A_{lm}U_l(r', E_l) + B_{lm}\dot{U}_l(r', E_l) + C_{lm}U_l(r, E_l))Y_{lm}(r') \tag{2.12.1}$$

To obtain the coefficients A_{lm}, B_{lm}, and C_{lm}, we need to satisfy two conditions for the function ϕ_{lo}.

2.12.3 The concept of FP-LAPW

In the linearized augmented plane wave with the full potential (FP-LAPW) method[121], no approximations are made for the shape of the potential or charge density. Instead, they are preferably expanded in terms of lattice harmonics within each atomic sphere and Fourier series in the interstitial regions. This ensures the continuity of the potential at the surface of the muffin-tin sphere and it is developed in the following form:

$$\rho(r) = \begin{cases} \sum_k \rho_k e^{ikr}, & r > r_\alpha \\ \sum_{lm} \rho_{lm}(r) Y_{lm}(r), & r < r_\alpha \end{cases} \tag{2.12.2}$$

2.13 WIEN2k code

The package of software called WIEN2k consists of set of programs, is commonly utilized to calculate the properties of matters. Wien2K has advanced features like the ability to perform calculations with spin-orbit coupling and model effects of strong electron correlations using the FP-LAPW method. It is only compatible with UNIX (LINUX) operating

systems and was developed in FORTRAN90. It was created at Vienna University of Technology in Austria by Karlheinz Schwarz and Peter Blaha [146] The code was initially made available in 1990 under the name WIEN90, and has subsequently received modifications in the form of WIEN93, WIEN95, WIEN97, and, most recently, WIEN2K [147]. With each successive release, additional features and enhancements were introduced.

2.13.1 Initialization (Computational Detail)

The first stage of initialization is creating an input file named *Case.struct* that provides details about the structure, such as the network type, space group, cell parameters (a, b and c in Bohr or (Å)), and atom positions inside the cell. The next step is to do initialization after inputting the parameters or data of any material into the *structGen* page. Once the *case.struct* file is generated, the initialization can be completed using the "$init - lapw$" command line, which requires starting a number of minimal auxiliary processes that will create inputs for the main programs.[147]:

► **NN:**

the file *case.struct* determines the atomic coordination of specific cell. To make sure the atomic spheres don't overlap, use a separation between the nearest neighbors within a certain distance (usually set to 2). Following that, the distances between these closest neighbors are recorded in a different file called *case.outputnn*.

► **LSTART:** By integrating the atomic densities and figuring out how to handle various orbitals in band structure calculations, the charge density of the crystal is produced. It also needs a cutoff energy level, commonly set at -6.0 Ry, to discriminate between core states and valence states.

► **SYMMETRY:** By utilizing the details available including lattice type and atomic positions, the generation of symmetry operations for the spatial group, corresponding to individual atomic sites, and calculates the matrices representing the corresponding rotation operations.

► **KGEN:** Produce unique mesh of K-points within the irreducible part of the first Brillouin zone (BZ).

► **DSTART:** Create a initial density for the self-consistent cycle (SCF cycle) of the atomic densities overlapped that produced in LSTART.

2.13.2 Self-consistent cycle (SCF)

The following program is for calculating SCF cycle, which is the process lunched and it stops until the solution converges:

► **LAPW0:** Computing the potential as sum of the Coulomb potential V_C and the V_{xc} [147].

► **LAPW1:** responsible for determining the eigenvalues, and eigenvectors, with the results being saved in the *case.vector* file[147].

► **LAPW2:** calculation of the valence charge density, which are made up of the electron densities within each MT sphere[147].

► **LCORE:** calculate core states and densities[147].

► **MIXER:** mixes input and output densities[147].

The diagram below (2.4) shows the steps necessary to process the file.struct using Wien2K code.

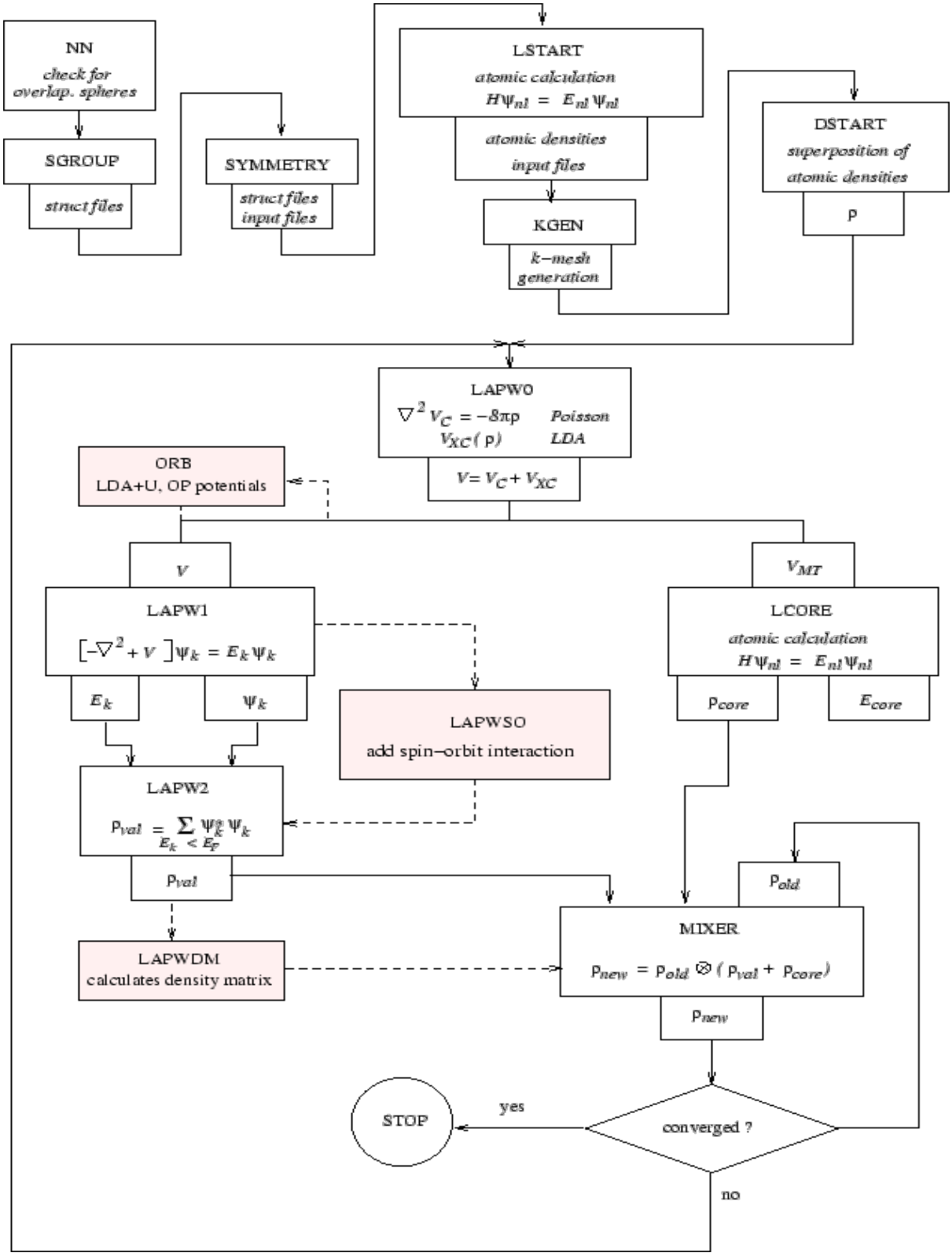

Figure 2.4: Wien2k structure[147].

2.14 The structure of Prediction Diagnostic Software (SPuDs)

2.14.1 Initialization

The computational tool SPuDS, developed by M. Lufaso[148], can predict the crystal structures of perovskites, including those that have undergone distortion due to BO_6 tilting. The software can be installed and operated on Windows operating systems. The interface of SPuDS allows users to specify a given composition and initiate calculations that can optimize the structure in ten different Glazer tilt systems for simple perovskites and seven systems for double perovskites, as discussed in Chapter (1), to determine the optimal structure based on the user's input and composition. The following steps explain the procedure for using the program:

▶ Entering each ion of the prdicted atom in each site.

▶ Clicking the calculate icon that shows.

▶ The findings will appear in two files "**gii.txt**" and "**output.txt**", the first one illustrate the instability index based on every Glazer tilting, and output.txt file includes the basic information about structure as , lattice canstant, positions, bond valence, space group, and other data.

Chapter 3

RESULTS

► Computational details.

► Structural properties of $BaRERuO_6$ (Gd, Er and Tm).

► Section (1): electronic, magnetic and optical properties of Ba_2GdRuO_6 double perovskite.

► Section (2): electronic, magnetic and magneto-optical of Ba_2RERuO_6 (RE= Er, Tm) double perovskite.

3.1 Introduction

The prediction for new materials has the potential to enhance and advance technological applications. By utilizing simulations with various codes and algorithms, we can gain valuable insights into the physical properties of materials and obtain results that closely correspond to experimental data.

The chapter is structured into two distinct sections, categorized according to the electronic properties of the materials under investigation. The initial section delves into the physical attributes of Ba_2GdRuO_6 materials, which display advantageous optoelectronic characteristics. The subsequent section centers its attention on the Ba_2RERuO_6 (RE= Er, and Tm) material, which exhibits noteworthy magneto-optical properties.

3.2 Computational details

First-principle (DFT) analysis was used to examine the structural, electronic, magneto-optical, magnetic, and optical properties of Ba_2RERuO_6(RE=Gd, Er, and Tm) compounds. Moreover, we used the method of FP-LAPW and were handled by the code of WIEN2k[147]. The correlation and exchange functionals were described using the general gradient method (GGA) [114, 115]. Additionally, the Hubbard Coulomb-site correction[118] (GGA+U) was utilized for modifying $4f$ and $4d$ localized shells in order to provide a more efficient electronic property description. The U values of each atom were chosen from literature as follows: $(4f)-(6\ \text{eV})$ for Er and Tm, also $(4f)$-(7.07 eV) for Gd, and $(4d)-(3\ \text{eV})$ for Ru [21, 149]. We have also added the spin-orbit coupling (SOC) to perform magneto-optical calculations. Several parameters were checked to complete the calculation. We have restricted the propagation of plane waves to (RMT) $k$max= 7 (cutoff parameter), and RMT-Gmax= 12 for the charge density. The maximum angular momentum for the expansion of the wave function in the muffin-tin sphere was restricted to a specific value $l_{max} = 10$. The cutoff energy was set at -6.0 Ry, and the criterion for the total energy convergence was about 0.0001 Ry. In order to sample the first Brillouin zone (BZ), a total of 3000 and 5000 points, which is equivalent to 244 points, in the

reciprocal space of the Brillouin zone, were determined. In comparison, a dense mesh of 405 points was chosen for the calculation of magneto-optical and optical properties, which is necessary to achieve convergence of the total energy in the self-consistent calculation. This corresponds to a mesh size of $14 \times 14 \times 14$, and $17 \times 17 \times 17$.

3.3 Structural properties of $BaRERuO_6$ (Gd, Er and Tm)

In their ideal form, double perovskite materials display a cubic structure; nevertheless, this cubic system can distort owing to a number of factors, as discussed in the first chapter. In this investigation, we used Goldschmidt's tolerance factor to quantify the degree to which the deformed cubic structure diverges from the original, as well as to calculate the possibility of double perovskites octahedral distortion. It referred to be "t", as exemplified by the following [50]:

$$t = \frac{(r_{Ba} + r_O)}{\sqrt{2}(\frac{(r_{Gd}+r_{Ru})}{2}+r_O)} \tag{3.3.1}$$

Each atom has r ionic radii as follows [25]: $r_{Ru}(Ru^{5+})$= 0.57 Å, $r_{Gd}(Gd^{3+})$=0.938 Å, $r_{Er}(Er^{3+})$= 0.89 Å, $r_{Tm}(Tm^{3+})$= 0.88 Å, , $r_{Ba}(Ba^{2+})$ = 1.61 Å and $r_O(O^{2-})$= 1.40 Å. The t factor result for these compounds are t = 0.999 for Ba_2ErRuO_6, t = 1.001 for Ba_2TmRuO_6 and t = 0.99 for Ba_2GdRuO_6. In general, the t factor for the stability of the double perovskite structure ranges from $0.78 < t \leq 1.05$ [148].

As a consequence, the crystal structure of Ba_2GdRuO_6, Ba_2ErRuO_6 and Ba_2TmRuO_6 compounds belongs to a face centered cubic $Fm\bar{3}m$ (no; 225), with a = b = c, $\alpha = \beta = \gamma = 90°$ [29, 150] with no octahedra tilting ($a^0a^0a^0$).

Table 3.1: The electronic configuration of each element as follow

Ba:[Xe]$6s^2$	Ru:[Kr]$4d^75s^1$	O: $1s^22s^22p^4$
Gd:[Xe]$4f^75d^16s^2$	Er: [Xe]$4f^{12}6s^2$	Tm:[Xe]4f136s^2

The atomic positions for the three materials are shown in the table (3.2).

The stability of the magnetic phase

: In order to accurately characterize the physical properties of double perovskite compounds using the FP-LAPW method, it is imperative to ascertain the fundamental energy state, which represents the minimum energy of the system. To determine the total energy with respect to the volume of the individual crystal unit, we employed auto-coherent computations to solve the Kohn-Sham equations. The figures (3.1, 3.2, and 3.3) show the optimal structure for each material depends on the minimum ground state energy for each: antiferromagnetic(AFM), ferromagnetic (FM), nonmagnetic (NM) orderings.

In the context of antiferromagnetic (AFM), the order of (RE ↑, Ru ↓) is considered, where the material's magnetic moment is zero. Furthermore, in the ferrimagnetic phase (FiM), the spins of the two atoms are oriented in opposite directions and have different magnitudes, resulting in a non-zero net magnetic moment for the material. In the ferromagnetic configuration (FM), the atoms are oriented parallel in the same direction (RE ↑, Ru ↑), as shown in figure (3.4). For nonmagnetic (NM) phases, the material's total magnetic moment is equal to zero, because the spin magnetic moments of the atoms are ignored. The spin of barium and oxygen is disregarded due to their significantly lower magnetic moments compared to those of gadolinium, erbium, thulium and ruthenium.

According to the curves depicted in Figures (3.1, 3.2, and 3.3), it can be observed that the energy of the ground state is at its minimum in the ferrimagnetic phase for the materials Ba_2ErRuO_6, Ba_2GdRuO_6, and Ba_2TmRuO_6. Therefore, these materials exhibit ferrimagnetic properties (These materials exhibit non-zero total magnetic moments).

The data was fitted using the Birch-Murnaghan equation, employing the GGA method. [151, 152]:

$$E(V) = E_0 + \frac{9B_0V_0}{16}\{[\frac{V_0}{V}^{\frac{2}{3}} - 1]B' + [V(\frac{V_0}{V})^{\frac{2}{3}} - 1]^2 + [6 - 4(\frac{V_0}{V}^{\frac{2}{3}})]\} \tag{3.3.2}$$

V_0, the volume at equilibrium, represents the equilibrium volume, while E_0 represents the corresponding total energy, which is the minimum total energy. B represents the equilibrium compressibility modulus, and $B^{'}$ represents its pressure derivative.

The estimated parameters of Ba_2RERuO_6 (Gd, Er and Tm) compounds are presented

in the table (3.3), including the lattice constant (a), total energy balance in the ground state E_0, bulk modulus (B) and their derivative B'.

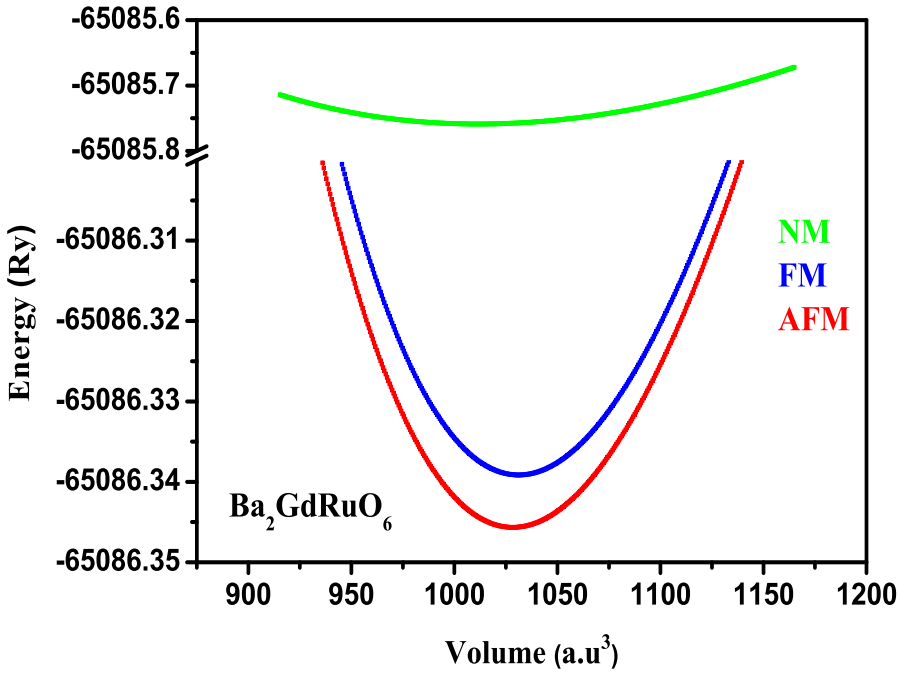

Figure 3.1: Optimized structure of Ba_2GdRuO_6 double perovskites.

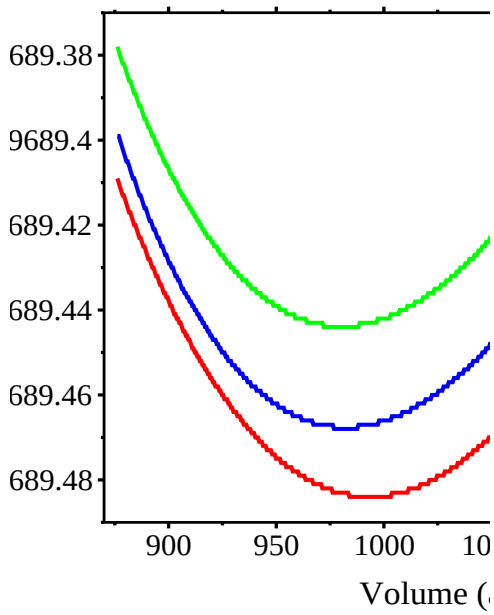

Figure 3.2: Optimized structure of Ba_2TmRuO_6 double perovskites.

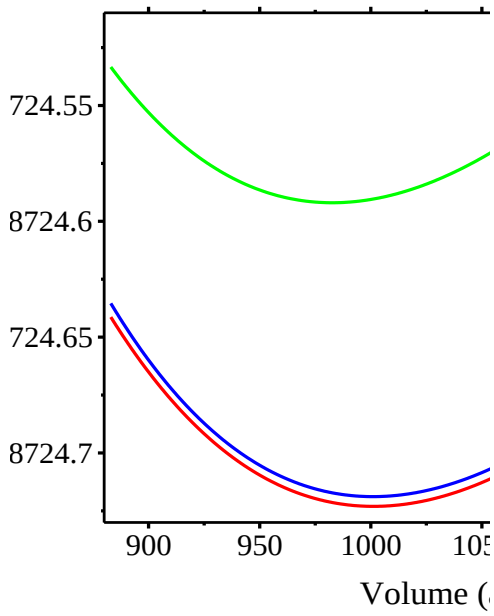

Figure 3.3: Optimized structure of Ba_2ErRuO_6 double perovskites.

Table 3.2: Atomic positions of Ba_2ErRuO_6(RE= Gd, Er, and Tm) perovskites.

Ba_2GdRuO_6				Ba_2ErRuO_6				Ba_2TmRuO_6			
Atoms	x	y	z	Atoms	x	y	z	Atoms	x	y	z
Ba	0.25	0.25	0.25	Ba	0.25	0.25	0.25	Ba	0.25	0.25	0.25
Gd	0.5	0.5	0.5	Er	0.5	0.5	0.5	Tm	0.5	0.5	0.5
Ru	0	0	0	Ru	0	0	0	Ru	0	0	0
O	0.2688	0	0	O	0.236348	0	0	O	0.237061	0	0

Table 3.3: Lattice Constant (a_0), Volume (V), Bulk modulus (B) and its derivative B' and E_0 of Ba_2RERuO_6 (RE= Gd, Er and Tm), respecetivly [153, 154].

Parameters		Ba_2GdRuO_6	Ba_2ErRuO_6	Ba_2TmRuO_6
a_0 (Å)	GGA	8.4787[154], 8.42[26]	8.4034[153], 8.323[150]	8.3816[153], 8.2878[29]
	SPuDs[148]	8.5112	8.4678	8.4478
V (a.u.)^3		1028.3141	1001.1976	993.3930
B (GPa)		134.4058	137.1875	138.5501
B'		4.6130	4.3582	2.2357
$E_0(Ry)$		-65086.3456	-68724.723	-69689.484

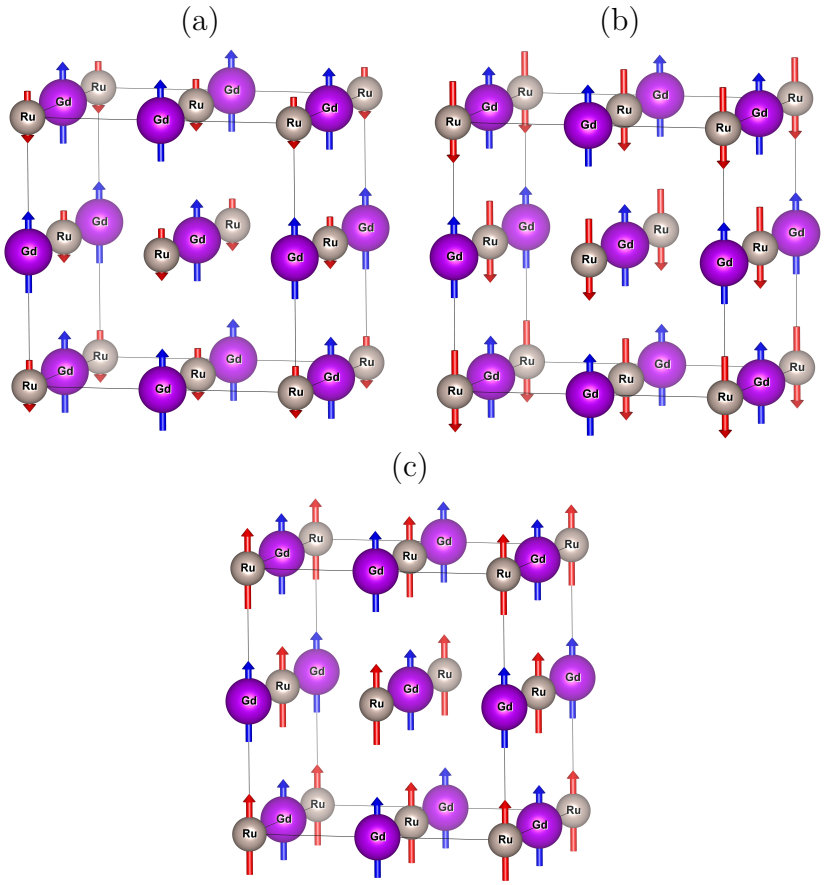

Figure 3.4: Magnetic configurations: (a) ferrimagnetic (FiM), (b) antiferromagnetic (AFM), (c) ferromagnetic (FM).

Section (1): electronic, magnetic and optical properties of Ba_2GdRuO_6 double perovskite

Until now, the optoelectronic device industry, such as solar cells, requires materials with specific features. As an initial step, we will investigate the physical properties of Ba_2GdRuO_6 through first-principles simulation work. This section will explore the potential of this material to display notable attributes in photovoltaic devices.

3.4 Electronic properties

The theory of electronic states is a crucial framework for comprehensively understanding the chemical and physical properties of materials in their solid state. The investigation of materials heavily relies on the behaviour of electrons, with the electronic population state, band structure, and electron density serving as fundamental parameters for characterizing their electronic properties. In this particular study, we aim to examine the electronic properties of the compound, namely Ba_2GdRuO_6, under the condition of the absence of octahedral distortion phenomena. It is worth noting that the crystal structure of these compounds exhibits symmetry solely in the form of $Fm\bar{3}m$ (No 225). The computed total density of states (TDOS) and band structure of the double perovskite compound Ba_2GdRuO_6 are shown in Figure (3.5).

3.4.1 Density of states (DOS)

According to TDOS, the Ba_2GdRuO_6 material is a semiconductor in both spin channels. The partial density of states (PDOS) offers information on the individual contributions of every single atom in the structure. According to PDOS in figure (3.5-(a)), the Ru-4d sub-shells (D_{t2g}/ D_{eg}) contributed to the minimal of the (VB) with the 2p-orbitals (O atom) within the range of values of -6 to -4 eV for both spin channels. Additionally, the 4f (Gd atom) shells at -2 eV made a considerable contribution to the PDOS band

for spin-up states. The significant hybridization occurred at the Fermi level between the Ru-D_{t2g} and O-2p shells, besides the hybridization of the 4f (Gd atom) and the 2p (O atom) shells.

The Hubbard potential U effects are visible in the PDOS obtained from the GGA+U computation, as illustrated in figure (3.5-(b)); an; an observed phenomenon is the augmentation of the localization bands of the 4f and 4d orbitals, which can be attributed to the influence of the Hubbard potential U. Furthermore, the PDOS demonstrates that the unoccupied 4f orbitals are displaced towards higher energy levels by approximately 6.5 eV in the spin-down state. Conversely, in the spin-up state, the Gd-4f and Ru-Dt2g orbitals experience shifts towards -5.8 eV and 2 eV, respectively. Furthermore, it can be observed that the energy gaps of the spin-up and spin-down states increase to 3.42 eV and 1.316 eV, respectively.

3.4.2 Energy bands structure

The energy levels accessible to an electron are dictated by the manner in which energy bands are represented in reciprocal space vector k. Moreover, the band structure profiles determined from the GGA calculation in figure (3.6-(a)) have been calculated along high symmetric lines in the Brillouin zone. Highlight the presence of two separate band gap characteristics for both channels. Conduction band minimum and valence band maximum differences in a spin-down channel imply a direct band gap nature, with a minimum VB of about 0 eV and a maximum CB of about 2.46 eV in the Brillouin zone, resulting in a band gap energy of 2.464 eV. On the other hand, there is an indirect band gap $\Gamma-X$ with a band gap energy of about 1.024 eV in the direction of the spin-up channel. We performed a GGA+U calculation, which considers the electronic correlation between the Gd(4f) and Ru(4d) electrons exclusively. In the figure (3.6-b), the information presented depicts the computed band structure along the high-symmetry paths within the first Brillouin zone using GGA+U. The results indicate differences in the band structure.

The Ba_2GdRuO_6 compound exhibits an indirect (direct) semiconductor band gap along the Γ-X (X) direction, with the valence band maximum located at the Γ point and the conduction band minimum at the X point in spin-down channels(spin up channels),

respectively.

The figure (3.6-b) illustrates the displacement of the $4f$ orbitals of the Gd atom, resulting in the splitting of the sub-shell in both spin channels. The Hubbard potential also affects the Ru-4d (D_{t2g}) states, causing them to shift towards the conduction band (CB) in the spin-up channels. The contribution of both the $4f$ (spin down channels) and the 4d orbitals significantly influences the conduction band and determines the magnetic moments.

Table 3.4: A comparison of our work's band gap with that of other semiconductors employed in optoelectronic devices.

Materials	E_g (eV)	Direct/ Indirect
Ba_2GdRuO_6	1.024 ↑; 2.464 ↓ (GGA)[154]	Γ-X; X-X
	1.316 ↑; 3.42↓ (GGA+U)[154]	
$Cs_2AgInBr_6$	1.427 (B3LYP)[155]	(Γ-Γ)
$CH_3NH_3PbI_3$	1.6 (DFT)[156]	/
$Cs_2AgBiBr_6$	1.32 (GGA)[157]	(L-Γ)
MA_2AgBiX_6 (I, Br)	1.64; 2.1 (EXP)[8]	/
$Cs_2AgBiBr_6$	2.16 (EXP)[8]	/

(a)

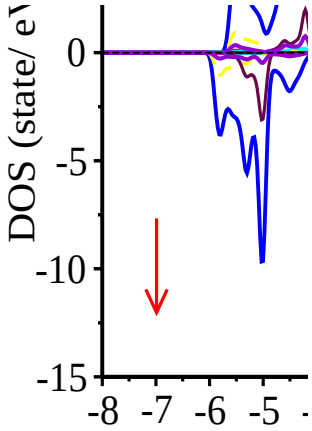

(b)

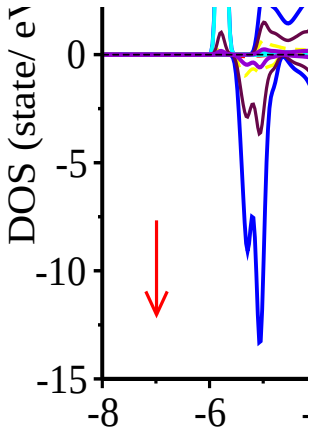

Figure 3.5: TDOS and PDOS of Ba_2GdRuO_6 material, within GGA and GGA+U calculations.[154]

(a)

(b)

Figure 3.6: Band structure of Ba_2GdRuO_6 material, within GGA and GGA+U calculations[154].

3.5 Magnetic properties:

According to our information, there is no theoretical or empirical study indicating the magnetic moment or magnetic phase of Ba_2GdRuO_6. Therefore, our magnetic results for this material are predictions and can serve as data for further theoretical or experimental studies in the future.

The GGA approximation is used to optimize the antiferromagnetic (AFM), nonmagnetic (NM), and ferromagnetic (FM) orderings of the Ba_2GdRuO_6 material to obtain the stable magnetic phase (Figure 3.1). The table (3.5) contains the total, interstitial, and local magnetic moments determined through the GGA and GGA+U approaches. For these methods described, the total magnetic moment is approximately 3.9 μ_B. An increase in the magnetic moment of both Gd and Ru within GGA+U without modifying the magnetic alignment appeared from the local magnetic moment of each atom. In addition, the total magnetic moment is produced by the atoms of gadolinium and ruthenium, which contribute more to electronic transitions than barium and oxygen atoms (see Figure 3.5). In addition, predicting the magnetic nature of materials based solely on the magnetic nature of atoms is not advisable due to the potential for phase transitions. Furthermore, as shown in Table 3.5, some magnetic moment values reported in the literature for the Gd and Ru atoms are compared to our findings[21, 158–160]. The ferrimagnetic configuration in which the spins of Ru and Gd are antiparallel is indicated by the negative value of the interstitial magnetic moment. The negative values of the magnetic moment of the Ru cations on-site B' decrease the total magnetic moment and confirm that they are aligned in an antiparallel manner with the cations. Additionally, the Weiss model [161] justifies that alignment, stating that the orientation of antiparallel order results from the ferromagnetic interaction of each sub-lattice with the ferrimagnetic arrangement of the lattice, which indicates a long-range interaction Ru−O−Gd−O−Ru than the short-range interaction Gd−O−Ru. Most likely as a result of the poor orbital mixing among lanthanide and transition metal ions [25].

Table 3.5: magnetic moments (μ_B) of Ba_2GdRuO_6 material[154].

	m_{int}	m_T	m_{Ba}	m_{Gd}	m_{Ru}	m_O
GGA	-0.465	3.999	-0.012	6.817	-1.670	-0.109
			−0.00241 [162]	6.726 [21]	1.20 [160]	
				7.94 [163]		
GGA+U	-0.446	3.999	-0.010	6.937	-1.833	-0.105
				6.754 [21]	2.87 [163]	
					-1.873 [159]	

3.6 Optical properties

Perovskites are currently the subject of extensive research due to their exceptional optical properties, which make them highly desirable for applications in photovoltaics[57].

The complex dielectric function, which relies on the frequency ω, is often used to characterize the optical properties, which is described as [164]:

$$\epsilon(\omega) = \epsilon_1(\omega) + i\epsilon_2(\omega) \tag{3.6.1}$$

The real part (ϵ_1) and the imaginary part (ϵ_2) form the dielectric function. The magnitude of polarization caused by an applied electric field is represented by ϵ_1. In contrast, the quantity of photons absorbed by a material is represented by ϵ_2 and could be determined using the momentum matrix element. ϵ_1 can be calculated using the Kramers-Kronig relations [21]. For a given frequency *omega*, the dielectric function components ϵ_1 and ϵ_2 can be shown separately:

$$\epsilon_2(\omega) = \frac{16\pi e^2}{\omega^2} \sum_s \vec{\lambda}\langle O|\vec{\nu}|s\rangle|^2 \delta(\omega - \Omega^2) \tag{3.6.2}$$

The matrix element $\langle O|\vec{\nu}|s\rangle$ indicates the optical transition from valence (VB) to conduction (CB) states, $\vec{\lambda}$ is the incoming light's polarization vector, ω is its frequency, and

Ω is the volume of the elementary cell [165].

$$\epsilon_1(\omega) = 1 + \frac{2}{\pi} p \int_0^\infty \frac{\omega' \epsilon_2(\omega')}{(\omega')^2 - (\omega)^2} d\omega' \tag{3.6.3}$$

The Cauchy principal value integral, represented by p, relates $\alpha(\omega)$, $k(\omega)$, $n(\omega)$, and $R(\omega)$, which are absorption coefficient , extinction coefficient refractive index, and reflectivity, respectively, to the dielectric function components [166, 167], where are provided as:

$$\alpha(\omega) = \frac{\sqrt{2}\omega}{c}(-\epsilon_1(\omega) + \sqrt{\epsilon_1^2(\omega) + \epsilon_2^2(\omega)})^{\frac{1}{2}} \tag{3.6.4}$$

$$k(\omega) = \frac{1}{\sqrt{2}}(-\epsilon_1(\omega) + \sqrt{\epsilon_1^2(\omega) + \epsilon_2^2(\omega)})^{\frac{1}{2}} \tag{3.6.5}$$

$$n(\omega) = \frac{1}{\sqrt{2}}(\epsilon_1(\omega) + \sqrt{\epsilon_1^2(\omega) + \epsilon_2^2(\omega)})^{\frac{1}{2}} \tag{3.6.6}$$

$$R(\omega) = |\frac{\sqrt{\epsilon(\omega)} - 1}{\sqrt{\epsilon(\omega)} + 1}|^2 \tag{3.6.7}$$

Based on the band structures, it is possible to confirm the nature of the optical gap for Ba_2GdRuO_6 in the spin-up channels. The figure (3.7) displays the real part $\epsilon_1(\omega)$ and imaginary part $\epsilon_2(\omega)$ of dielectric functions throughout the energy variation from 0 to 10 eV for each GGA and GGA+U calculations. The findings illustrate that the GGA and GGA+U approximations provide distinct values for the dielectric constant's real component, $\epsilon_1(0)$, with values of about 9.45 and 7.73, respectively. The imaginary component, ϵ_2, is in charge of calculating the optical gap energy, which indicates the starting point of material absorption and is determined to be 1.18eV for GGA and 1.6eV for GGA+U, respectively. Additionally, negative ϵ_1 values show that the material Ba_2GdRuO_6 appears to have total reflection metallic characteristics in the energy range of 7.25 to 10 eV. The observed negative values could potentially be ascribed to the presence of a substantial reflection region.

The GGA and GGA+U calculations reveal that $\epsilon_2(\omega)$ of Ba_2GdRuO_6 has three notable peaks with values of 9.05, 9.09, and 10.52 around 2.71eV (457.5 nm), 5.53eV (224.2 nm), and 7.16eV (173.2 nm). These peaks, however, are displaced inside GGA+U to 2.95 eV (8.17), 5.72 eV (10.31), and 6.73 eV (11.6). It would be more useful in applications involving the ultraviolet and visible light spectra. According to the partial density of states

(PDOS) in Figure (3.5), these peaks refer to the interband transitions. Figure 3.8 displays the absorption coefficient $\alpha(\omega)$ as a function of photon energy; this is proportionate to the imaginary component $\epsilon_2(\omega)$ as demonstrated in 1.5.4 equation. $\epsilon_2(\omega)$ and $\alpha(\omega)$ have extremely similar forms. The reported optical band gap energies agreed with the electronic band gap around 1.18eV and 1.6eV for GGA and GGA+U, respectively. The absorption spectrum has three highest peaks: value of 4.3 10^5 cm^{-1} around 2.86 eV, also, 9.6 10^5 around 5.66 eV, and 1.9 10^6 cm^{-1} around 7.96 eV, these energies correspond to (155.6 nm), (433.5 nm), and (218.9 nm), respectively. The absorption near the threshold is primarily attributed to the significant contributions of the optical transition channels between the RE-f/O-p orbitals and the Ru-d/O-p conduction bands orbitals. These high absorption coefficients were remarkable in organic-inorganic hybrid perovskites, allowing for the reduction in thickness of these materials, which this characteristic facilitates easy fabrication and low cost[57]. These findings exhibit similarities to the results obtained from lead and lead-free halide double perovskite materials, as presented in the table(3.6) [168–171].

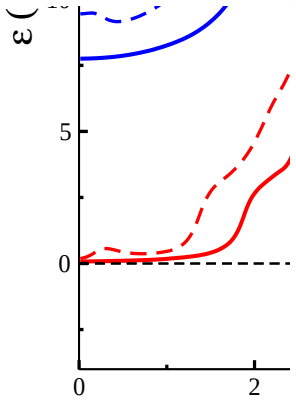

Figure 3.7: $\epsilon_1(\omega)$ the real component, and $\epsilon_2(\omega)$ imaginary Dielectric function for Ba_2GdRuO_6 material[154].

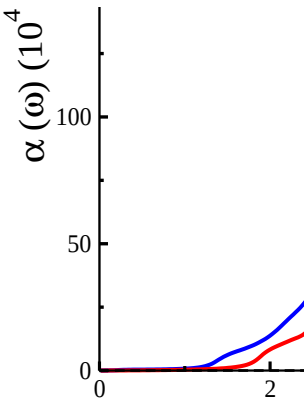

Figure 3.8: Coefficient of absorption for Ba_2GdRuO_6 compound[154].

The calculated σ represents the optical conductivity of the Ba_2GdRuO_6 material. Therefore, it is illustrated in figure (3.9). The optical conductivity changes appear to be approximately the same according to both approaches; however, it increases as photon energies pass the energy gap of optical edge, reaching its highest at 2.735 eV ($3.242.10^3$), 5.7 eV ($6.883.10^3$), and at 7.269 eV ($1.021.10^4$) $\Omega^{-1}.cm^{-1}$. As a consequence, this material's wavelength range occurs in both the visible and ultraviolet light spectrums.

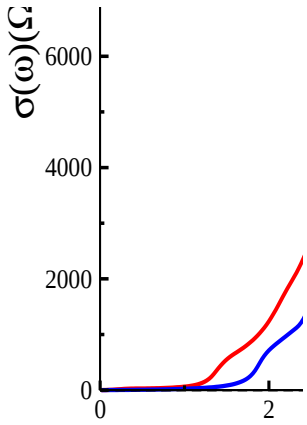

Figure 3.9: Optical conductivity of Ba_2GdRuO_6[154].

Figure (3.11-b) depicts the complex refractive index $\tilde{n}(\omega) = n(\omega) + ik(\omega)$, where $n(\omega)$ denotes the real component, and $k(\omega)$ denotes the imaginary part, also known as the extinction coefficient. The relationship among $\tilde{n}$ and α is shown in Figure (3.11-b), which shows that as the refractive $n(\omega)$ increases, the absorption $\alpha(\omega)$ decreases and vice versa. The static refractive index for GGA and GGA+U, given as $n(0) = \sqrt{\epsilon_1}$, are respectively 3.07 and 2.78, falling within the range of values for Si (3.42) [168]. The $k(0)$ value remains zero until it reaches the absorption edge, at which time it begins to increase, as seen in Figure (3.11-c). It is essential to keep in mind that there is a relationship between $k(\omega)$, $\alpha(\omega)$, and $\epsilon_2(\omega)$, which may be written as $\alpha(\omega) = \frac{2\omega k(\omega)}{c}$ [167], this explains why the three spectra's forms are similar.

Furthermore, in Figure (3.11-c), the reflectivity $R(\omega)$ is displayed; it demonstrates how much light is reflected when it comes into connection with a material surface. Surface quality is shown by static reflectivity $R(0)$ values of 25.7% (GGA) and 22% (GGA+U). At higher energies, the Ba_2GdRuO_6 compound has the greatest reflectivity values, reaching 48.5% (GGA) and 46.7% (GGA+U). Furthermore, the visible spectrum reflectivity values

vary from 22% to 33%, demonstrating the material's capacity to reflect incoming solar energy.

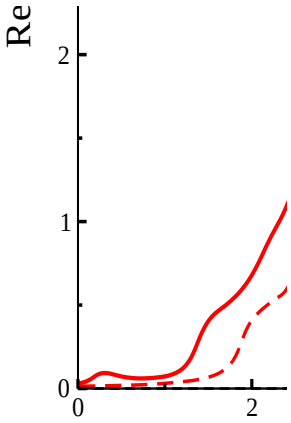

Figure 3.10: Represent the complex refractive index: $n(\omega)$, and $k(\omega)$ for Ba_2GdRuO_6 material[154].

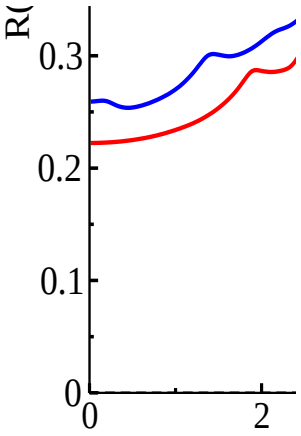

Figure 3.11: The reflectivity $R(\omega)$ of the Ba_2GdRuO_6 material[154].

Table 3.6: Comparing our Ba_2GdRuO_6 material work's optical properties to earlier theoretical studies.

Materials		ϵ_0^1	$\sigma_{max}{}^{(\Omega^{-1}.cm^{-1})}$	n_0	R_0	$\alpha_{max}(10^6)^{(cm^{-1})}$
Ba_2GdRuO_6	(GGA,GGA+U)	9.45, (7.73)	9.8 10^3, (10^4)	3.07, (2.78)	0.25	1.8
Ba_2ErTaO_6	(DFT[34])	/	6 10^3	6.8	0.14	1.6
Ba_2ZnMoO_6	(TB-mBJ)[172]	4.26	5.7 10^3	2.05	0.12	1.9
$Cs_2AgInBr_6$	(GGA)[157]	/	/	2.09	/	0.3
Pb_2ScBiO_6	(GGA)[173]	7.1	9 10^3	2.7	0.21	1.64
Ba_2InTaO_6	(GGA)[8]	4.04	2.01	0.11	0.21	/

Section (2): electronic, magnetic and magneto-optical of Ba_2RERuO_6 (RE= Er, Tm) double perovskite

3.7 Electronic properties

3.7.1 Hubbard potential of Ruthenium (Ru) element Computational details:

Figure (3.12) illustrates the process of determining the Hubbard potential values for Ru metal using the computational details described earlier. The figure (3.12) illustrates the changes in the total magnetic moment and gap energy of the element Ru as the Hubbard potential varies from 1 to 4 eV. The rare earth elements Erbium (Er) and Thulium (Tm) are considered to have a value of 6 eV.

In materials that contain rare earth and transition metals, the Coulomb repulsion on site is strong enough to localize the electrons [174, 175]. The GGA approximation, however, is unable to anticipate the necessary splitting of f-states and d-states for such compounds because it cannot accurately characterize the exchange potential. There are many other methods used to correct this issue. In our research, we utilized the GGA+U[176] method [176] to improve the electronic structure of these materials. The choice of using the Hubbard potential for each state is based on the calculation of different U values. Figure 3.12 displays the magnetic moment and band gap energy of both compounds as a function of U potential. The curves illustrate the values of magnetic moment and band structure within the range of 1−4 eV. From the curves, we can observe that the magnetic moment and band gap increase and then stabilize at 3 eV and 4 eV for both compounds. The figures (3.13) and (3.14) represent the band structure and total density of states of both compounds, Ba_2TmRuO_6 and Ba_2ErRuO_6. From the figures, the compounds exhibited a transition from metallic to semiconductor behaviour for Ba_2ErRuO_6 and half-metallic behaviour for Ba_2TmRuO_6 for U = 3 eV with band gap energy increases from 0 eV to 1.24 eV and 1.25 eV at U = 3 eV, for Ba_2ErRuO_6 and Ba_2TmRuO_6, respectively, the results are shown in table (3.7). Based on these electronic results, we can conclude that

U = 3 eV is the threshold value that causes this compound to transition from a metallic nature to a half-metallic or semiconductor material. This value has been determined for the Ru atom by other studies[5].

Figure 3.12: The total magnetic moment, and band gap energy of Ru vary as a function of the Hubbard potential U for (a): Ba_2ErRuO_6, (b):Ba_2TmRuO_6[153].

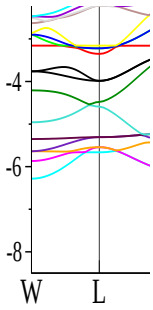
-4
-6
-8
W
L

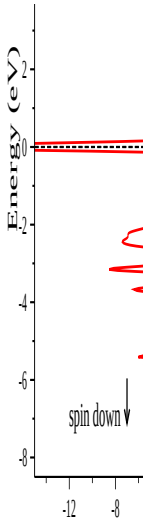
Energy (eV)
2
0
-2
-4
-6
-8
spin down
-12
-8

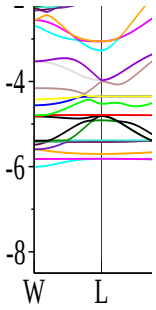
-4
-6
-8
W
L

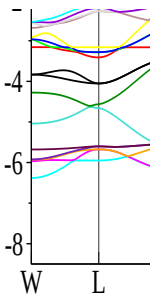
-4
-6
-8
W
L


Energy (eV)
2
0
-2
-4
-6
-8
spin down
-12
-8

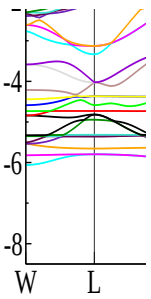
-4
-6
-8
W
L

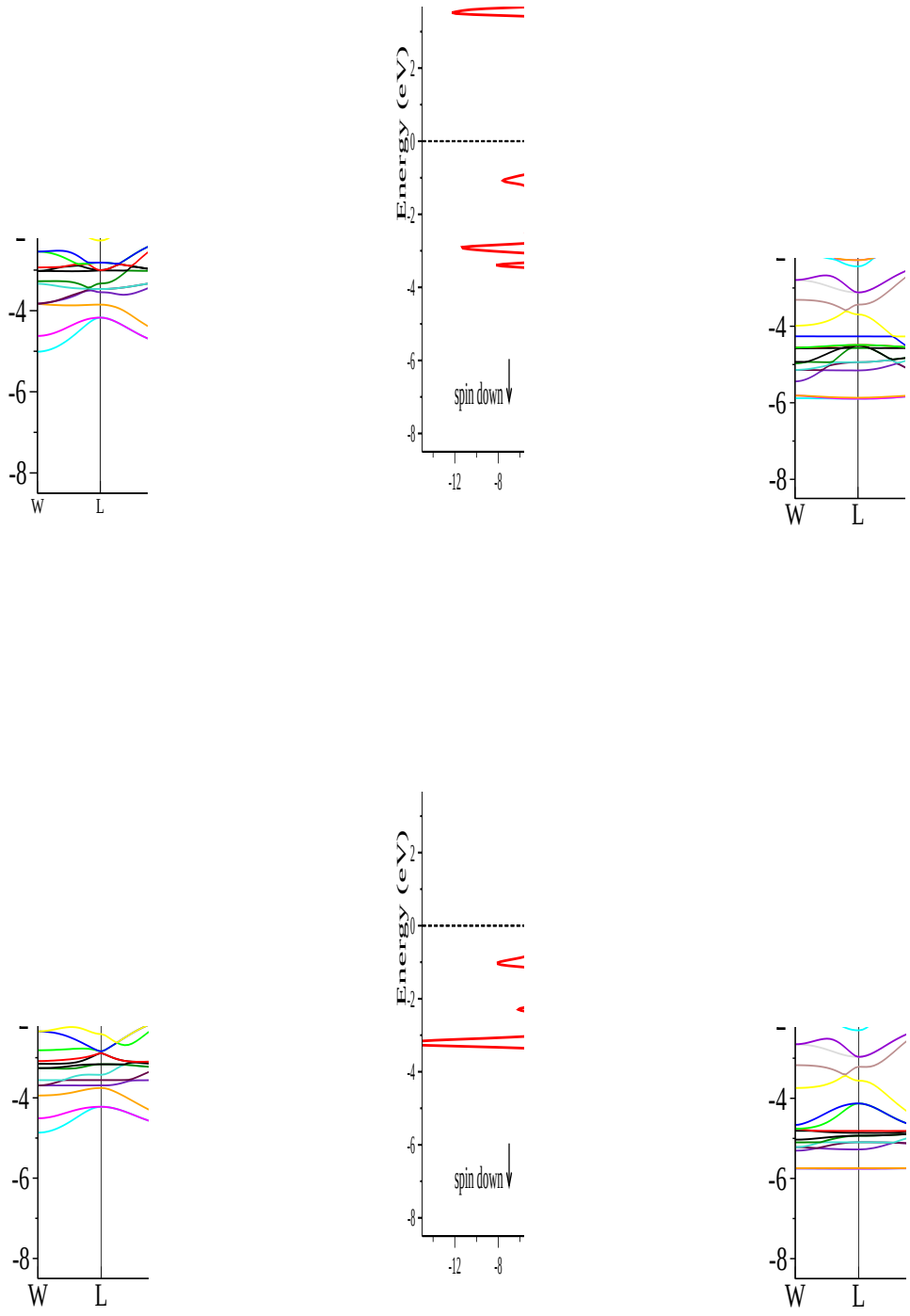

Figure 3.13: band structure and density of states of Ba_2ErRuO_6 compound, for different U potential (U= 1, 2, 3 and 4 eV).

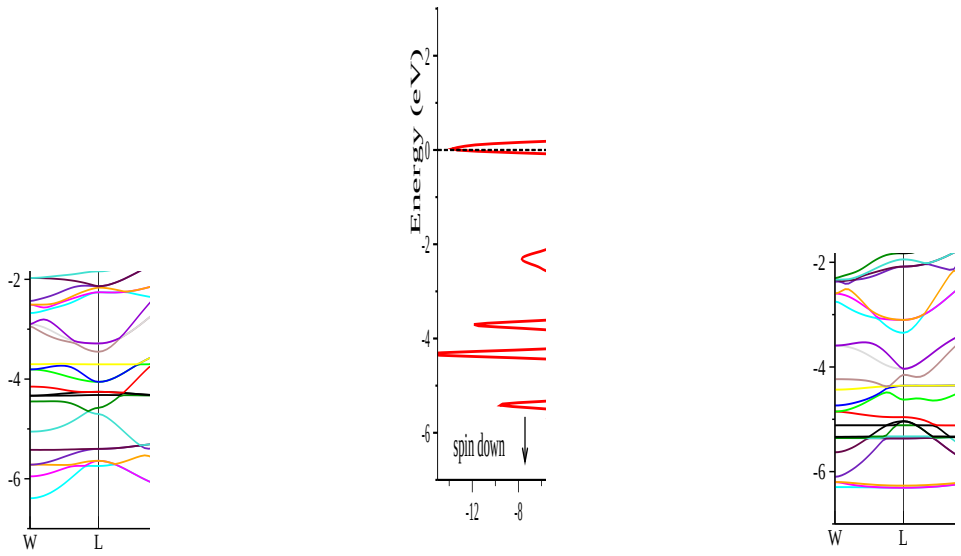
Energy (eV)
spin down
W
L

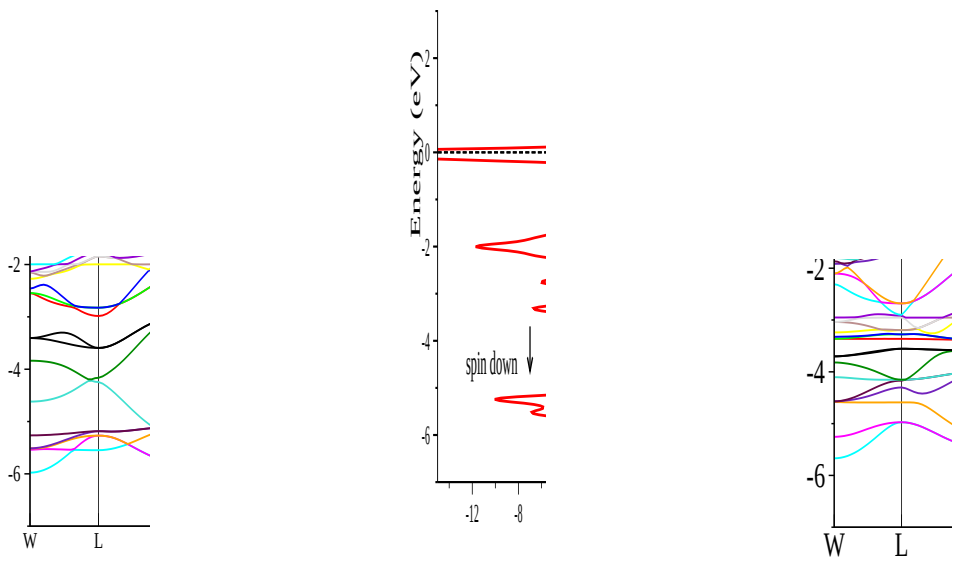
Energy (eV)
spin down
W
L

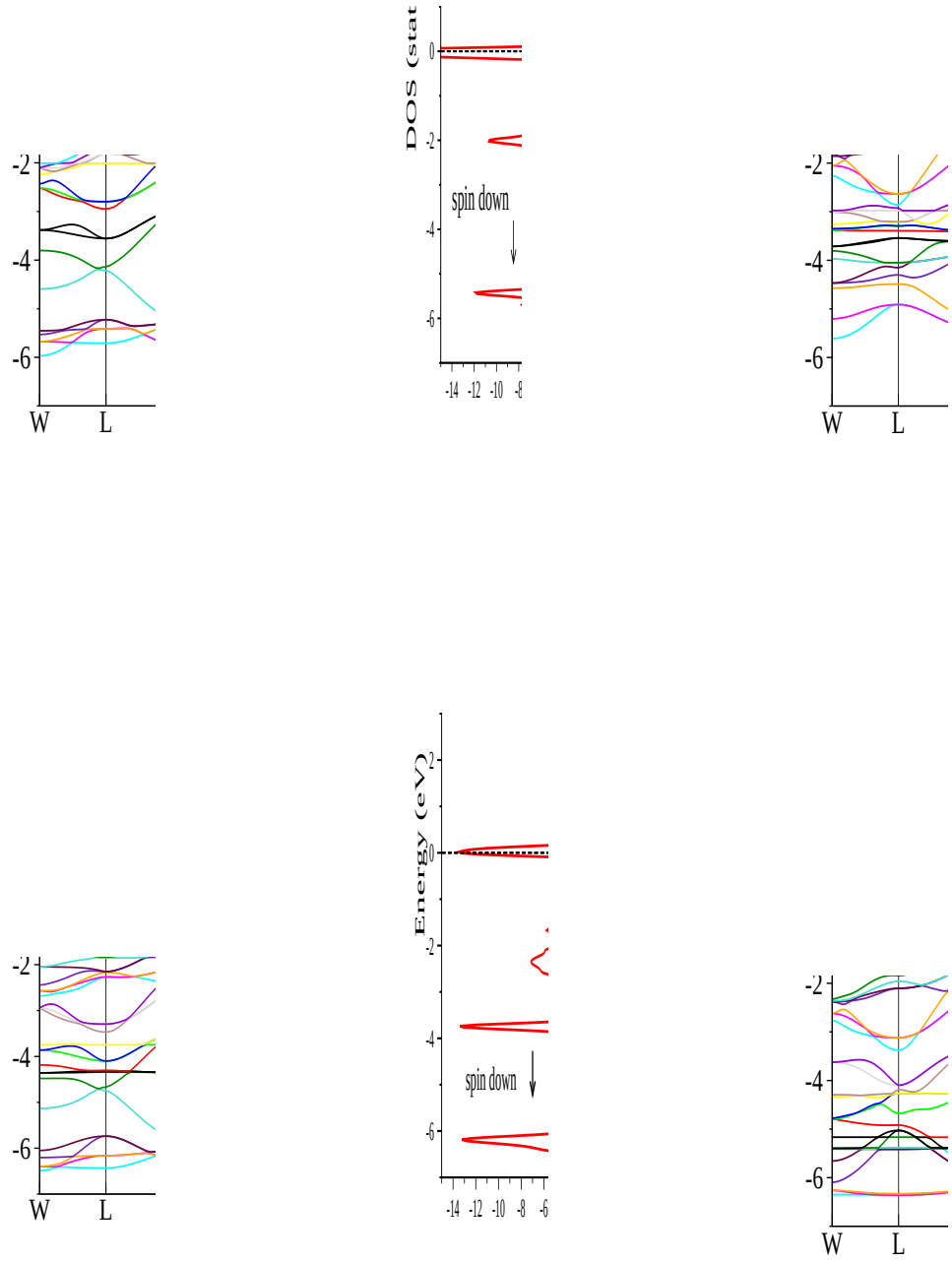

Figure 3.14: TDOS and band structure of the compoundBa_2TmRuO_6, for different U(Ru) potential (U= 1, 2, 3 and 4 eV).

Table 3.7: The total magnetic moment and band gap energy of Ba_2RERuO_6 (RE = Er, Tm) at different Hubbard potential.

	U (eV)	1	2	3	4
Ba_2ErRuO_6	E_g(eV)	-	-	1.24	1.37
	m_{μ_B}	0.36	0.05	6.00	6.00
Ba_2TmRuO_6	E_g(eV)	-	1.089	1.25	1.41
	m_{μ_B}	0.756	0.91	1.00	1.00

3.7.2 Band structure and density of states (DOS):

The total (TDOS) and the partial density of state (PDOS), along with the band structure results, are considered vital for the analysis of the electronic structure of the FiM phase of these double perovskites Ba_2RERuO_6 (RE = Er, and Tm) materials.

To begin, the figure (3.16)-(a, b) illustrates the TDOS, using both GGA and GGA+U approximations. In GGA calculation, for both materials, the metallic behaviour is clearly observed as a result of a significant overlap in their energy states near the Fermi level. We could confirm from analysis of the PDOS and band structure as shown in figures (3.16), (3.13-c), and (3.14-c). There is a vital contribution at the Fermi level E_f of 4f-(RE atoms) and 4d-Dt_{2g} orbitals of ruthenium, and the overlap between the 4d Dt_{2g}-2p, 4f (RE), and 2p-O orbitals is what leads to metallic nature of these materials.

Figure 3.15: TDOS and PDOS of Ba_2ErRuO_6 and Ba_2TmRuO_6 using GGA method.

Figure 3.16: TDOS and PDOS of Ba_2ErRuO_6 and Ba_2TmRuO_6 using GGA+U method.

The contribution of O(2p) and Ru(D_{eg}, Dt_{2g}) orbitals, which are expanded in between -6 and -4 eV, is additionally apparent at the valence band (VB), which extends from -4 to -1

eV. The majority of spin states are mainly composed of 4f-(RE atoms) and 2p-(O atoms) electronic states, and due to being filled up of Er(Tm^{+3})↑. Meanwhile, the Ba orbitals do not contribute to the VB. The contribution of Ru(D_{eg}) in the conduction band (CB), however, exhibits a noticeable peak at 3.5 eV at the top area of the CB.

The Ba-4d electrons have a contribution that lies between 5 and 8.5 eV. Furthermore, with the GGA+U, the TDOS is illustrated in figure 3.16(c, d). The Hubbard potential has an influence on the overall density of state by the electronic structure of the Ba_2TmRuO_6 and Ba_2ErRuO_6 systems from metallic to half-metallic and semiconductor, respectively, according to change the U potential value until correcting the localized 4f rare earth and 4d metal transition. We obtained the correct U Hubbard, which was 3 eV for Ru atoms and 6 eV for Er and Tm.

The Ba_2ErRuO_6 compound's crystalline structure clearly exhibits a semiconductor nature, with both direct and indirect (Γ-X) band gaps in majority and minority spin states with gap energy values equal to 3.089 eV and 1.249 eV, respectively, as illustrated in figure (3.13-c). The structure's nature of Ba_2TmRuO_6 exhibits a semi-metallic character, with a direct band gap (X) in majority-spin channels of 1,259 eV. From PDOS result, the RE-4f and Ru-4d states have to shift away from their Fermi level positions, which the field of the crystal dividing the 4f-(RE^{3+}) orbitals into three non-degenerate sub-levels and the 4d-(Ru^{5+}) orbitals into two sub-level groups (Dt_{2g}) and (D_{eg}). The dominant peak around the Fermi level, as depicted in figure 3.16-(c), is made up primarily of $Dt2g$-(Ru) orbitals in majority spin states, with a weak hybridization of 2p-(O atoms) for the Ba_2ErRuO_6. Furthermore, a compound in Ba_2TmRuO_6, the figure 3.16-(d) reveals that the Fermi level is occupied by 4f(Tm atoms) orbitals in minority-spin channels, which are in charge of the metallic behaviour. While 4f, 4d, and 2p orbitals hybridize in the energy range of 1 to 6 eV in the VB, Er(Tm)-4f, Ru-4d, and O-2p orbitals peak in the CB at 2.5 eV and Ru(D_{eg}) becomes conductive at roughly 3eV. The responsible states for the electronic transitions in these materials are the RE-4f and Ru-4d orbitals.

3.8 Magnetic properties

The magnetic properties provide us with specific information about the level of magnetism in a material compared to another through the calculation of the magnetic moment, which is a crucial indicator of magnetism. The spin magnetic moments, both total and local, of these compounds are calculated using the GGA and GGA+U methods. The results are presented in table (3.8). The above results demonstrate that our compounds exhibit ferrimagnetic behaviour with a total magnetic moment of 2.30 (0.43) ν_B (GGA) for Ba_2ErRuO_6 and Ba_2TmRuO_6, respectively. This value is the sum of the partial moments associated with each atom. The Ba and O atoms show a minimal contribution to the total magnetic moment, with nearly negligible values, as indicated in the table (3.8). The primary contributions to the total magnetic moment arise from the erbium and thulium atoms, where their magnetic moment is 2.83 μ_B, 1.72 μ_B (GGA), and 2.93 μ_B and 1.89 μ_B (GGA+U) for Ba_2ErRuO_6 and Ba_2TmRuO_6 respectively.

The negative values of the magnetic moment of the Ru atoms on the B site decrease the total magnetic moment and confirm that they are aligned antiparallel to the RE cations. The antiferromagnetic (ferrimagnetic) behaviour observed in Ba_2RERuO_6 can be primarily attributed to long-range superexchange interactions involving the RE-O-Ru-O-RE pathways rather than the short-range RE-O-Ru interactions; this; this can be explained by the weak orbital mixing between lanthanide and transition metals[25]. There exist both FM (ferromagnetic) and AFM (antiferromagnetic) contributions to the exchange coupling, which is contingent upon the magnitude of the local Coulomb interaction U. The magnetic interactions are exceedingly responsive to even minor alterations in the positions of the ligands. The introduction of U into the system leads to a slight reduction in the equilibrium lattice constant and a 90-degree Er-O-Ru bond angle. Consequently, it is reasonable to expect that the coupling constant may change sign, causing a reversal in the magnetic configuration from ferromagnetic (FM) to antiferromagnetic (ferrimagnetic) and vice versa. Furthermore, the utilization of the GGA+U method yields a more significant magnetic moment compared to the GGA method. This can be attributed to the fact that U promotes the localization of f and d-states and diminishes p-d hybridiza-

tion, thereby increasing magnetic moments. The spin polarization P for the Ba_2TmRuO_6 compound at Fermi level is 100 % of GGA+U, is given with [59]:

$$P = \frac{\mid N_{(\uparrow)} - N_{(\downarrow)} \mid}{\mid N_{(\uparrow)} + N_{(\downarrow)} \mid} \tag{3.8.1}$$

Where the Fermi level density of states is represented by $N_\uparrow$ and $N_\downarrow$, the 4f (Tm atoms) and 4d-(Ru atoms) orbitals (see table 3.8) are primarily responsible for the magnetization at the Fermi level.

Table 3.8: Total and local magnetic moments (μ_B) for the double perovskites Ba_2RERuO_6(Er, Tm), within GGA and GGA+U methods.

		Ba_2ErRuO_6					Ba_2TmRuO_6			
	m_{tot}	m_{Ba}	m_{Er}	m_{Ru}	m_{O}	m_{tot}	m_{Ba}	m_{Tm}	m_{Ru}	m_{O}
	2.30	-0.002	2.83	-0.42	-0.001	0.43	-0.004	1.72	-0.79	-0.046
GGA		0.005[23]								
		0.062[23]	2.78[177]		1.72[177]		0.09[177]			
			2.98[23]							
GGA + U	6.00	0.01	2.96	1.90	0.11	1.00	-0.01	1.89	-1.84	-0.07
		0.006[23]	2.96[23]	2.87 [160]	0.0024[23]			1.70[177]	1.20[29, 150]	0.09[177]
			4.43 [160]					1.91 [160]	2.13 [160]	

3.9 Magneto-Optical properties:

The Kerr effect can be examined from the figure (3.17). As we can see, for Kerr rotation θ_k, the maximum points for the compounds Ba_2ErRuO_6 and Ba_2TmRuO_6 are around 17.7° and 5.6° situated at 0.23 eV and 0.2 eV, respectively. A similar behaviour was found in $Co_3Sn_2S_2$ ferromagnetic material with huge Kerr of 3.2° and Faraday rotation

of 9.4° [178]. The topological electronic structure is thought to be responsible for these enormous values in the infrared spectrum. In addition, we observe that the second peak of Kerr rotation is located at 2.91 eV with 6° for Ba_2ErRuO_6 and at 2.78 eV with a value equal to 2° for Ba_2TmRuO_6. To contrast with other theoretical calculations like Ba_2FeMO_6 (M = W, Re, and Mo), whereby the major amplitude of each compound's Kerr rotation is 1.7° at 2.83 eV, 1.51° at 1.54 eV, and 1.46° at 0.87 eV [4]. It is also important to note how Kerr rotation varies with respect to Kerr ellipticity(ϵ_k): at the maximum of the Kerr rotation spectrum, the ϵ_k spectrum crosses the zero line, which is consistent with the Kramers-Kronig relation [179]. The primary peaks of the Kerr ellipticity is 11.09° (3.17 eV) for Ba_2ErRuO_6 and 2.9° (0.51 eV) for Ba_2TmRuO_6.

The optical diagonal and off-diagonal conductivity, which are connected to the inter-band and intra-band transitions, have to be calculated in order to study the magneto-optical Kerr effects [180].

The optical conductivity, absorption σ^1_{xx}, and dispersive σ^2_{xx} parts in the energy range of 0 to 10 eV are shown in the figure (3.18). The two compounds exhibit a modest peak in the infrared region of about 0.15 eV, which is caused by intra-band transitions of d states and inter-band transitions between p with d and f orbitals. The intra-band transition at higher energies was missed because of its small amplitude [59, 181], while inter-band transitions exclusively generate the other peaks in the 2 to 8.5 eV range. In figure 3.19, the off-diagonal conductivity σ_{xy} is displayed.

The values of θ_k and Kerr ellipticity ϵ_k, which are contrary to diagonal conductivity, are proportional to off-diagonal conductivity (equation 1.5.4) [4, 60]. It becomes obvious that the highest Kerr rotation, θ_{max}, corresponds to the maximum peak in σ_{xy}, $\omega\sigma_{xy}$, (shown in figures 3.19, 3.20) and to smaller diagonal conductivity σ_{xx}.

Figure 3.17: Polar Kerr rotation θ_k and Kerr ellipticity ϵ_k as a function of energy for (a)Ba_2ErRuO_6 and (b) Ba_2TmRuO_6.

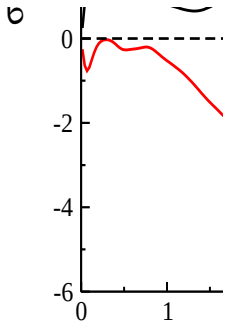

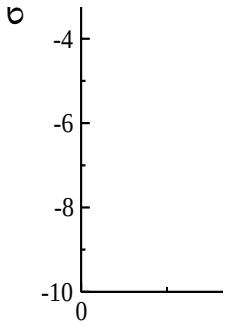

Figure 3.18: Absorption real part σ_{xx}^{1} and dispersive optical conductivity imaginary part σ_{xx}^{2} of (a) Ba_2ErRuO_6 and (b) Ba_2TmRuO_6.

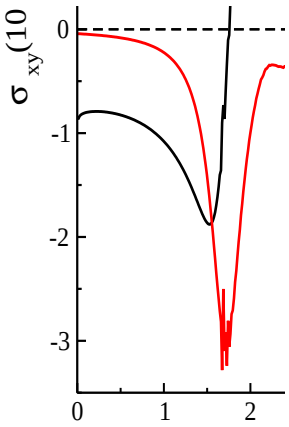

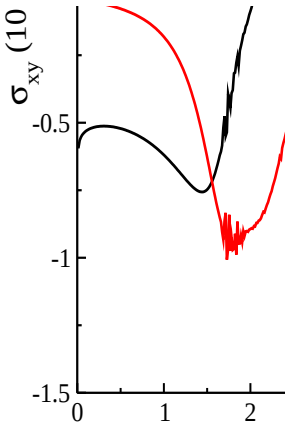

Figure 3.19: Real σ^1_{xy} and imaginary σ^2_{xy} parts (off-diagonal conductivity tensor) for (a) Ba_2ErRuO_6 and (b) Ba_2TmRuO_6.

Figure 3.20: Complex off-diagonal conductivity for (a)Ba_2ErRuO_6 and (b)Ba_2TmRuO_6.

GENERAL CONCLUSION

In the current thesis, a series of first-principle calculations were conducted. These calculations were performed using a Wien2K code. In our study, we employed the (GGA) approximation to determine the most stable phase of each material and identify the precise magnetic orders. We have discovered that Ba_2GdRuO_6, Ba_2ErRuO_6 and Ba_2TmRuO_6 remain stable in the ferrimagnetic phase due to the total magnetic moments is not equal to zero. The total magnetic moment of each compound is primarily attributed to the magnetic moment of rare earth atoms and ruthenium.

Applying the generalized gradient approximation (GGA) reveals that Ba_2GdRuO_6 possesses a semiconductor structure, while including GGA+U calculations results in an increasing band gap compared to the GGA calculation. The obtained results demonstrate that the optical properties of the double perovskite material (Ba_2GdRuO_6) are consistent with those of other optoelectronic materials. This material exhibits a narrow band gap of 1.024 (1.136) eV (for spin-up channels) for GGA (GGA+U) calculation, respectively, with absorption coefficient peaks observed at wavelengths of 457.5 nm and 173.2 nm.

We performed calculations on the band structure and density of states for the electronic properties. we employed the GGA+U approximation with U values of 6 eV for Er(Tm)-4f and 3 eV for Ru-4d electrons. Our calculations revealed that the Ba_2ErRuO_6 material exhibits a Semiconductor behaviour with an indirect band gap in the minority-spin states. In contrast, the Ba_2TmRuO_6 material displays a half-metallic character with an indirect band gap in the majority-spin states, with exhibits a polarization of 100%. These characteristics suggest that both materials possess the potential for a significant magneto-optical Kerr effect, with peak angles at $\theta_k = 17.7°$, $5.6°$ and $\epsilon_k = 11.09°$, $2.9°$ for Ba_2ErRuO_6 and Ba_2TmRuO_6, respectively. The two materials, Ba_2ErRuO_6 and Ba_2TmRuO_6, exhibit promising characteristics that render them excellent candidates for utilization in spintronics, optical switching and other applications.

Ultimately, it is essential to note that the GGA+U method employed in this study for Ba_2ErRuO_6 and Ba_2ErRuO_6 materials cannot accurately describe the dielectric tensor. Therefore, to accurately address the excited state properties, it is necessary to employ methods based on many-body perturbative schemes. It has been reported that these two compounds have the potential for giant magneto-optical Kerr effects (MOKEs). This is

the first time such potential has been observed in these compounds.

Regarding its optical properties, the compound Ba_2GdRuO_6 shows potential as a novel material for applications in renewable energy technologies, specifically within optoelectronics. However, further research is required to explore its capabilities and challenges in this field fully.

Bibliography

[1] JDR Tilley. *Perovskites: structure-property relationships*. John Wiley & Sons, (2016).

[2] G George, SR Ede, and Z Luo. *Fundamentals of perovskite oxides: synthesis, structure, properties and applications*. CRC Press, (2020).

[3] Y Shimakawa, M Azuma, and N Ichikawa. Multiferroic compounds with double-perovskite structures. *Materials*, 4(1):153–168, (2011).

[4] R Vidya, P Ravindran, A Kjekshus, and H Fjellvag. Huge magneto-optical effects in half-metallic double perovskites. *Physical Review B*, 70(18):184414, (2004).

[5] AP Sakhya, DP Rai, Md Sheikh, Sariful, M Mukherjee, A Dutta, and TP Sinha. Origin of the optical anisotropy and the electronic structure of Ru-based double perovskite oxides: Dft and xps studies. *RSC advances*, 7(69):43531–43539, (2017).

[6] HKM Rubel, A Miura, T Takei, N Kumada, M A-Mozahar, M Nagao, S Watauchi, I Tanaka, K Oka, and M Azuma. Superconducting double perovskite bismuth oxide prepared by a low-temperature hydrothermal reaction. *Angewandte Chemie*, 126 (14):3673–3677, (2014).

[7] HS Lu and GY Guo. Anomalous ferromagnetism and magneto-optical kerr effect in semiconducting double perovskite Ba_2NiOsO_6 and its (111)(Ba_2NiOsO_6)/$(BaTiO_3)$ 10 superlattice. *Physical Review B*, 100(5):054443, (2019).

[8] MS Shadabroo, H Abdizadeh, and MR Golobostanfard. Elpasolite structures based on A_2AgBiX_6 (A:MA,Cs,X:I,Br): Application in double perovskite solar cells. *Materials Science in Semiconductor Processing*, 125:105639, (2021).

[9] IH Al-Lehyani. A first-principle study of the stability and electronic properties of halide inorganic double perovskite Cs_2PbX_6 (X=Cl,I) for solar cell application. *Arabian Journal of Chemistry*, 14(2):102920, (2021).

[10] E Fertitta, S Das, D Banerjee, Ebrahimi, C Barraud, K Du, H Tian, CJ Pickard, C Weber, R Ramesh, et al. Study of disorder in pulsed laser deposited double perovskite oxides by first-principle structure prediction. *npj Computational Materials*, 7(1):1–8, (2021).

[11] V Verma, NP Patel, KVR Murthy, and M Srinivas. Photoluminescence of Eu (III) doped double perovskite phosphor for red led application. (2021).

[12] A Bhorde, R Waykar, SR Rondiya, S Nair, G Lonkar, A Funde, NY Dzade, et al. Structural, electronic, and optical properties of lead-free halide double perovskite Rb_2AgBiI_6: A combined experimental and dft study. *ES Materials & Manufacturing*, 12:43–52, (2021).

[13] A Kojima, K Teshima, Y Shirai, and T Miyasaka. Organometal halide perovskites as visible-light sensitizers for photovoltaic cells. *Journal of the american chemical society*, 131(17):6050–6051, (2009).

[14] KT Butler, JM Frost, and A Walsh. Band alignment of the hybrid halide perovskites $CH_3NH_3PbCl_3$, and $CH_3NH_3PbI_3$. *Materials Horizons*, 2(2):228–231, (2015).

[15] A Walsh. Principles of chemical bonding and band gap engineering in hybrid organic-inorganic halide perovskites. *The Journal of Physical Chemistry C*, 119 (11):5755–5760, (2015).

[16] C Lan, S Zhao, T Xu, Ma, S Hayase, and T Ma. Investigation on structures, band gaps, and electronic structures of lead free La_2NiMnO_6 double perovskite materials for potential application of solar cell. *Journal of Alloys and Compounds*, 655:208–214, (2016).

[17] MS Sheikh, AP Sakhya, R Maity, A Dutta, and TP Sinha. Narrow band gap and optical anisotropy in double perovskite oxide Sm_2NiMnO_6: a new promising solar cell absorber. *Solar Energy Materials and Solar Cells*, 193:206–213, (2019).

[18] M Kumar, A Raj, A Kumar, and A Anshul. Theoretical evidence of high power conversion efficiency in double perovskite solar cell device. *Optical Materials*, 111: 110565, (2021).

[19] L Corredor, J Téllez, J Pimentel, R Pureur, and J Rojas. Magnetic, structural and morphological characterization of Sr_2GdRuO_6 double perovskite. *J. Mod. Phys*, 2: 154–157, (2011).

[20] A Dutta, PK Mukhopadhyay, TP Sinha, S Shannigrahi, AK Himanshu, P Sen, and SK Bandyopadhyay. Sr_2SmNbO_6 perovskite: Synthesis, characterization and density functional theory calculations. *Materials Chemistry and Physics*, 179:55–64, (2016).

[21] S Berri, S Chami, M Attallah, M Oumertem, and D Maouche. Density functional studies of magneto-optic properties of Sr_2GdReO_6. *Modern Electronic Materials*, 4: 13, (2018).

[22] S Haid, B Bouadjemi, M Houari, M Matougui, T Lantri, S Bentata, and Z Aziz. Investigation of dft+u effect of holmium rare-earth on the electronic, magnetic and the half-metallic ferromagnetic properties of double perovskite Ba_2HoReO_6. *Solid State Communications*, 294:29–35, (2019).

[23] S Haid, M Matougui, S Benatmane, B Bouadjemi, M Houari, A Zitouni, T Lantri, and S Bentata. Predictive study of the rare earth double perovskite oxide Ba_2ErReO_6 and the influence of the hubbard parameter u on its half-metallicity. *Journal of Superconductivity and Novel Magnetism*, pages 1–11, (2021).

[24] A Nid-Bahami, A El Kenz, A Benyoussef, L Bahmad, M Hamedoun, and H El Moussaoui. Magnetic properties of double perovskite Sr_2RuHoO_6: Monte carlo simulation. *Journal of Magnetism and Magnetic Materials*, 417:258–266, (2016).

[25] S Vasala and M Karppinen. $A_2B'B''O_6$ perovskites: a review. *Progress in solid state chemistry*, 43(1-2):1–36, (2015).

[26] S Dani, A Arya, H Sharma, R Kumar, N Goyal, R Kumar, and R Pandit. Structural and electronic properties of double perovskite ruthenates; A_2GdRuO_6 (where A=Ba,Sr). *Journal of Alloys and Compounds*, 913:165177, (2022).

[27] NG Parkinson, PD Hatton, JAK Howard, C Ritter, RM Ibberson, and MK Wu. Variable temperature neutron powder diffraction study to determine the magnetic interactions in Sr_2LnRuO_6 (Ln=HoandTb). *Journal of Physics: Condensed Matter*, 16(43):7611, (2004).

[28] C Sakai, Y Doi, and Y Hinatsu. Crystal structures and magnetic properties of double perovskite compounds Ca_2LnRuO_6 (Ln=Y,La−−Lu). *Journal of alloys and compounds*, 408:608–612, (2006).

[29] Doi, Y Hinatsu, Y Nakamura, A aand Ishii, and Y Morii. Magnetic and neutron diffraction studies on double perovskites A_2LnRuO_6 (A=Sr,Ba;Ln=Tm,Yb). *Journal of Materials Chemistry*, 13(7):1758–1763, (2003).

[30] Y Hinatsu, Y Izumiyama, Y Doi, A Alemi, M Wakeshima, A Nakamura, and Y Morii. Studies on magnetic and calorimetric properties of double perovskites Ba_2HoRuO_6 and Ba_2HoIrO_6. *Journal of Solid State Chemistry*, 177(1):38–44, 2004.

[31] Y Hinatsu. Diverse structures of mixed-metal oxides containing rare earths and their magnetic properties. *Journal of the ceramic society of Japan*, 123(1441):845–852, (2015).

[32] RA De Groot, FM Mueller, PG v van Engen, and KHJ Buschow. New class of materials: half-metallic ferromagnets. *Physical review letters*, 50(25):2024, (1983).

[33] A Kumar, M Kumar, and RP Singh. Magnetic, opto-electronic, and thermodynamic properties of half-metallic double perovskite oxide,Ba_2YbTaO_6: a density functional theory study. *Journal of Materials Science: Materials in Electronics*, 32(10):12951–12965, (2021).

[34] M Nabi and CD Gupta. Study of the magneto-electronic, optical, thermal and thermoelectric applications of double perovskites Ba_2MTaO_6 (M=Er,Tm). *RSC advances*, 9(28):15852–15867, (2019).

[35] PM Oppeneer. Magneto-optical kerr spectra. *Handbook of Magnetic Materials*, 13: 229–422, (2001).

[36] MQ Cai, X Tan, GW Yang, LQ Wen, LL Wang, WY Hu, and YG Wang. Giant magneto-optical kerr effects in ferromagnetic perovskite $BiNiO_3$ with half-metallic state. *The Journal of Physical Chemistry C*, 112(42):16638–16642, (2008).

[37] N Zu, Q Zhang, J Hao, M Zhang, J Li, X Liu, and R Li. First-principles study on giant magneto-optical kerr effect in double perovskites$Sr_2BB'O_6$ (B=Cr,Mo,B'=W,Re,Os). *Journal of Solid State Chemistry*, page 123274, (2022).

[38] SA Mir and CD Gupta. Scrutinizing the stability and exploring the dependence of thermoelectric properties on band structure of 3d-3d metal-based double perovskites Ba_2FeNiO_6 and Ba_2CoNiO_6. *Scientific reports*, 11(1):1–13, (2021).

[39] F Galasso and W Darby. Ordering of the octahedrally coördinated cation position in the perovskite structure. *The Journal of Physical Chemistry*, 66(1):131–132, (1962).

[40] DAA Ahmed, S Bağcı, E Karaca, and HM Tütüncü. Elastic properties of ABF_3 (A:Ag,KandB:Mg,Zn) perovskites. In *AIP Conference Proceedings*, volume 2042, (2018).

[41] P Basera and S Bhattacharya. Chalcogenide perovskites (ABS_3; A=Ba,Ca,Sr;B=Hf,Sn): An emerging class of semiconductors for optoelectronics. *The Journal of Physical Chemistry Letters*, 13(28):6439–6446, (2022).

[42] GKL Goh, FF Lange, and CG . Haile, SM . Levi. Hydrothermal synthesis of $KNbO_3$ and $NaNbO_3$ powders. *Journal of materials research*, 18(2):338–345, (2003).

[43] RS Perez, TFT Cerqueira, S Korbel, S Botti, and SM Marques. Prediction of stable nitride perovskites. *Chemistry of Materials*, 27(17):5957–5963, (2015).

[44] SC Miller and WF Love. Tables of irreducible representations of space groups and co-representations of magnetic space groups. *(No Title)*, (1967).

[45] T Ishihara. *Perovskite oxide for solid oxide fuel cells*. Springer Science & Business Media, (2009).

[46] CJ Howard and HT Stokes. Structures and phase transitions in perovskites a group-theoretical approach. *Acta Crystallographica Section A: Foundations of Crystallography*, 61(1):93–111, (2005).

[47] AM Glazer, SA Mabud, and R Clarke. Acta crystallogr, sect. b: Struct. crystallogr. cryst. chem. (1972).

[48] MP Woodward. Octahedral tilting in perovskites. i. geometrical considerations. *Acta Crystallographica Section B: Structural Science*, 53(1):32–43, (1997).

[49] AM Glazer. Simple ways of determining perovskite structures. *Acta Crystallographica Section A: Crystal Physics, Diffraction, Theoretical and General Crystallography*, 31(6):756–762, (1975).

[50] WM Lufaso, WP Barnes, and MP Woodward. Structure prediction of ordered and disordered multiple octahedral cation perovskites using spuds. *Acta Crystallographica Section B: Structural Science*, 62(3):397–410, (2006).

[51] JC Howard and TH Stokes. Group-theoretical analysis of octahedral tilting in perovskites. *Acta Crystallographica Section B: Structural Science*, 54(6):782–789, (1998).

[52] WJ Yin, B Weng, J Ge, Q Sun, Z Li, and Y Yan. Oxide perovskites, double perovskites and derivatives for electrocatalysis, photocatalysis, and photovoltaics. *Energy & Environmental Science*, 12(2):442–462, (2019).

[53] XAV Moya, R Cardona, JIV Hernández, DA Téllez, and JJ Roa-Rojas. Electronic and crystalline structure, magnetic response, and optical characterization of rare-earth ruthenate Sr_2HoRuO_6. *Journal of Electronic Materials*, 47(7):3421–3429, 2018.

[54] G King and PM Woodward. Cation ordering in perovskites. *Journal of Materials Chemistry*, 20(28):5785–5796, (2010).

[55] Jakobus Hubertus Lambertus Voncken. *The rare earth elements: an introduction*. Springer, (2016).

[56] AS Arrott. Generalized curie-weiss law. *Physical Review B*, 31(5):2851, (1985).

[57] NS Arul and VD Nithya. *Revolution of Perovskite*. Springer, 2020.

[58] Y Izumiyama, Y Doi, M Wakeshima, Y Hinatsu, Y Shimojo, and Y Morii. Magnetic properties of the antiferromagnetic double perovskite Ba_2PrRuO_6. *Journal of Physics: Condensed Matter*, 13(6):1303, (2001).

[59] M Mahdi, A Djabri, MM Koc, R Boukhalfa, M Erkovan, Y Chumakov, and F Chemam. Ab initio study of $GdCo_5$ magnetic and magneto-optical properties. *Materials Science Poland*, 37, (2019).

[60] JL Erskine. Magneto-optical studies of ferromagnetic metals. In *AIP Conference Proceedings*, volume 24, pages 190–194, (1975).

[61] FJ Kahn, PS Pershan, and JP Remeika. Ultraviolet magneto-optical properties of single-crystal orthoferrites, garnets, and other ferric oxide compounds. *Physical review*, 186(3):891, (1969).

[62] K Sato and T Ishibashi. Fundamentals of magneto-optical spectroscopy. *Frontiers in Physics*, page 615, (2022).

[63] SD Stranks and HJ Snaith. Metal-halide perovskites for photovoltaic and light-emitting devices. *Nature nanotechnology*, 10(5):391–402, (2015).

[64] MdS Sheikh, D Ghosh, A Dutta, S Bhattacharyya, and TP Sinha. Lead free double perovskite oxides ln2nimno6 (Ln=La,Eu,Dy,Lu), a new promising material for photovoltaic application. *Materials Science and Engineering: B*, 226:10–17, (2017).

[65] AS Thind, S Kavadiya, M Kouhnavard, R Wheelus, SB Cho, LY Lin, C Kacica, HK Mulmudi, KA Unocic, AY Borisevich, et al. $KBaTeBiO_6$: a lead-free, inorganic double-perovskite semiconductor for photovoltaic applications. *Chemistry of Materials*, 31(13):4769–4778, (2019).

[66] Q Sun, J Wang, WJ Yin, and Y Yan. Bandgap engineering of stable lead-free oxide double perovskites for photovoltaics. *Advanced Materials*, 30(15):1705901, (2018).

[67] SJ Pearton, DP Norton, YW Heo, LC Tien, MP Ivill, Y Li, BS Kang, F Ren, J Kelly, and AF Hebard. Zno spintronics and nanowire devices. *Journal of electronic materials*, 35:862–868, (2006).

[68] C Felser and GH Fecher. *Spintronics: from materials to devices*. Springer Science & Business Media, 2013.

[69] A Singh, C Jansen, K Lahabi, and J Aarts. Growth of half-metallic CrO_2 nanostructures for superconducting spintronic applications. *arXiv preprint arXiv:1603.02675*, (2016).

[70] MS Ansari, MHD Othman, MO Ansari, S Ansari, and H Abdullah. Progress in Fe_3O_4 centered spintronic systems: Development, architecture, and features. *Applied Materials Today*, 25:101181, (2021).

[71] H Kato, T Okuda, Y Okimoto, Y Tomioka, Y Takenoya, A Ohkubo, M Kawasaki, and Y Tokura. Metallic ordered double-perovskite Sr_2CrReO_6 with maximal curie temperature of 635 k. *Applied physics letters*, 81(2):328–330, (2002).

[72] AJ Hauser, JR Soliz, M Dixit, REA Williams, MA Susner, B Peters, LM Mier, TL Gustafson, MD Sumption, HL Fraser, et al. Fully ordered Sr_2CrReO_6 epitaxial films: A high-temperature ferrimagnetic semiconductor. *Physical Review B*, 85(16): 161201, (2012).

[73] B Niu, F Jin, J Liu, Y Zhang, P Jiang, T Feng, B Xu, and T He. Highly carbon and sulfur tolerant Sr_2TiMoO_6-δ double perovskite anode for solid oxide fuel cells. *International Journal of Hydrogen Energy*, 44(36):20404–20415, (2019).

[74] JJA Flores, MLA Rodriguez, JVA Vera, JGR Quinones, SJG Martinez, and RA Zarraga. Advances in the knowledge of the double perovskites derived from the conformation and substitution of the material Sr_2MgMoO_6-δ as anode with potential application in sofc cell. *International Journal of Hydrogen Energy*, 46(51): 26152–26162, (2021).

[75] Y Tsutsumi. Schrodinger equation. *Funkcialaj Ekvacioj*, 30:115–125, (1987).

[76] Erwin Schrödinger. The schrodinger equation. *Phys Rev*, 28(6):1049–1070, (1926).

[77] M Born and R Oppenheimer. Zur quantentheorie der molekeln. *Annalen der physik*, 389(20):457–484, (1927).

[78] MT Huber. Zur theorie der beruhrung fester elastischer korper. *Annalen der Physik*, 319(6):153–163, (1904).

[79] DR Hartree. Representation of the exchange terms in fock's equations by a quasi-potential. *Physical Review*, 109(3):840, (1958).

[80] V Fock. Näherungsmethode zur lösung des quantenmechanischen mehrkörperproblems. *Zeitschrift für Physik*, 61:126–148, (1930).

[81] DR Hartree. The wave mechanics of an atom with a non-coulomb central field. part i. theory and methods. In *Mathematical Proceedings of the Cambridge Philosophical Society*, volume 24, pages 89–110, (1928).

[82] ND Lang and W Kohn. Theory of metal surfaces: charge density and surface energy. *Physical Review B*, 1(12):4555, (1970).

[83] VA Fock. Zs. f. phys. 61, 126 (1930);(b) va fock. *Proc. State Opt. Inst.(USSR)*, 5 (51):1–28, (1931).

[84] CJ Slater. Atomic shielding constants. *Physical Review*, 36(1):57, (1930).

[85] H Chermette. Density functional theory: a powerful tool for theoretical studies in coordination chemistry. *Coordination chemistry reviews*, 178:699–721, (1998).

[86] H Paulsen and XA Trautwein. Density functional theory calculations for spin crossover complexes. *Spin Crossover in Transition Metal Compounds III*, pages 197–219, (2004).

[87] NJ Harvey. Dft computation of relative spin-state energetics of transition metal compounds. *Principles and applications of density functional theory in inorganic chemistry I*, pages 151–184, (2004).

[88] HL Thomas. The calculation of atomic fields. In *Mathematical proceedings of the Cambridge philosophical society*, volume 23, pages 542–548, (1927).

[89] E Fermi. Statistical method to determine some properties of atoms. *Rend. Accad. Naz. Lincei*, 6(602-607):5, (1927).

[90] RG Parr and W Yang. Density-functional theory of the electronic structure of molecules. *Annual review of physical chemistry*, 46(1):701–728, (1995).

[91] AMP Dirac. Note on exchange phenomena in the thomas atom. In *Mathematical proceedings of the Cambridge philosophical society*, volume 26, pages 376–385, (1930).

[92] P Hohenberg and W Kohn. Inhomogeneous electron gas. *Physical review*, 136(3B): B864, (1964).

[93] W Kohn. Density functional and density matrix method scaling linearly with the number of atoms. *Physical Review Letters*, 76(17):3168, (1996).

[94] A Khouidmi et al. *Etude ab-initio des propriétés physiques des doubles pérovskites Ba_2BNbO_6 (B: Lanthanide).* PhD thesis, (2018).

[95] PR Antoniewicz and L Kleinman. Kohn-sham exchange potential exact to first order in ρ. *Physical Review B*, 31(10):6779, (1985).

[96] W Kohn and LJ Sham. Self-consistent equations including exchange and correlation effects. *Physical review*, 140(4A):A1133, (1965).

[97] AR Harris. Induction and dispersion forces in the electron gas theory of interacting closed shell systems. *The Journal of chemical physics*, 81(5):2403–2405, (1984).

[98] J Harris and RO Jones. The surface energy of a bounded electron gas. *Journal of Physics F: Metal Physics*, 4(8):1170, (1974).

[99] M Ernzerhof and GE Scuseria. Assessment of the perdew-burke-ernzerhof exchange-correlation functional. *The Journal of chemical physics*, 110(11):5029–5036, (1999).

[100] O Gunnarsson and IB Lundqvist. Exchange and correlation in atoms, molecules, and solids by the spin-density-functional formalism. *Physical Review B*, 13(10): 4274, (1976).

[101] CO Almbladh and AC Pedroza. Density-functional exchange-correlation potentials and orbital eigenvalues for light atoms. *Physical Review A*, 29(5):2322, (1984).

[102] A Savin, H Stoll, and H Preuss. An application of correlation energy density functionals to atoms and molecules. *Theoretica chimica acta*, 70(6):407–419, (1986).

[103] A Van de Walle and G Ceder. Correcting overbinding in local-density-approximation calculations. *Physical Review B*, 59(23):14992, (1999).

[104] A Souidi. *Etude des propriétés spintroniques du double Perovskite type $ABCO_6$*. PhD thesis, Université de Mostaganem-Abdelhamid Ibn Badis.

[105] NW Ashcroft and ND Mermin. *Solid state physics*. Cengage Learning, (2022).

[106] JP Perdew, ER McMullen, and A Zunger. Density-functional theory of the correlation energy in atoms and ions: a simple analytic model and a challenge. *Physical Review A*, 23(6):2785, (1981).

[107] A Zunger, JP Perdew, and GL Oliver. A self-interaction corrected approach to many-electron systems: Beyond the local spin density approximation. *Solid State Communications*, 34(12):933–936, (1980).

[108] PJ Perdew and W Yue. Accurate and simple density functional for the electronic exchange energy: Generalized gradient approximation. *Physical review B*, 33(12): 8800, (1986).

[109] DA Becke. Density-functional exchange-energy approximation with correct asymptotic behavior. *Physical review A*, 38(6):3098, (1988).

[110] Z Wu and RE Cohen. More accurate generalized gradient approximation for solids. *Physical Review B*, 73(23):235116, (2006).

[111] JP Perdew and Y Wang. Accurate and simple analytic representation of the electron-gas correlation energy. *Physical review B*, 45(23):13244, (1992).

[112] K Burke, JP Perdew, and Y Wang. Derivation of a generalized gradient approximation: The pw91 density functional. *Electronic Density Functional Theory: recent progress and new directions*, pages 81–111, (1998).

[113] JP Perdew, K Burke, and M Ernzerhof. Perdew, burke, and ernzerhof reply. *Physical Review Letters*, 80(4):891, (1998).

[114] JP Perdew, K Burke, and M Ernzerhof. Generalized gradient approximation made simple. *Physical review letters*, 77(18):3865, (1996).

[115] JP Perdew, K Burke, and M Ernzerhof. Generalized gradient approximation made simple (vol 77, pg 3865, 1996), (1997).

[116] Julien Claudot. *Développements et applications de méthodes pour la description de lénergie de corrélation dans les molécules et les solides*. PhD thesis, Université de Lorraine, (2018).

[117] SL Dudarev, GA Botton, SY Savrasov, CJ Humphreys, and AP Sutton. Electron-energy-loss spectra and the structural stability of nickel oxide: An LSDA≡U study. *Physical Review B*, 57(3):1505, (1998).

[118] IV Anisimov, J Zaanen, and KO Andersen. Band theory and mott insulators: Hubbard u instead of stoner i. *Physical Review B*, 44(3):943, (1991).

[119] A Chouiah. *Etude Ab-initio des Propriétés structurales, optoélectroniques, thermodynamiques et magnétiques des pérovskites*. PhD thesis, Université de Mostaganem, 2019.

[120] JB Goodenough. Spin-orbit-coupling effects in transition-metal compounds. *Physical Review*, 171(2):466, (1968).

[121] M Petersen, F Wagner, L Hufnagel, M Scheffler, P Blaha, and K Schwarz. Improving the efficiency of FP−LAPW calculations. *Computer Physics Communications*, 126(3):294–309, (2000).

[122] HL Skriver. *The LMTO method: muffin-tin orbitals and electronic structure*, volume 41. Springer Science & Business Media, 2012.

[123] MA Ghebouli, B Ghebouli, M Fatmi, and A Bouhemadou. Calculation of physical properties of the cubic perovskite-type oxide $BiScO_3$ using the pp-pw method based on the dft theory. *Solid state communications*, 151(12):908–915, (2011).

[124] H Eschrig, M Richter, and I Opahle. Relativistic solid state calculations. In *Theoretical and Computational Chemistry*, volume 14, pages 723–776. (2004).

[125] N Papanikolaou, R Zeller, and PH Dederichs. Conceptual improvements of the kkr method. *Journal of Physics: Condensed Matter*, 14(11):2799, (2002).

[126] GKH Madsen, P Blaha, K Schwarz, E Sjöstedt, and L Nordström. Efficient linearization of the augmented plane-wave method. *Physical Review B*, 64(19):195134, (2001).

[127] CJ Slater. Wave functions in a periodic potential. *Physical Review*, 51(10):846, (1937).

[128] JC Slater. Energy band calculations by the augmented plane wave method. In *Advances in quantum chemistry*, volume 1, pages 35–58. (1964).

[129] EP Blöchl. Projector augmented-wave method. *Physical review B*, 50(24):17953, (1994).

[130] OK Andersen, O Jepsen, and G Krier. Exact muffin-tin orbital theory. *Lectures on methods of electronic structure calculations*, pages 63–124, (1994).

[131] JD Singh and L Nordstrom. *Planewaves, Pseudopotentials, and the LAPW method*. Springer Science & Business Media, (2006).

[132] B Salhi et al. *Contribution a l'etude des proprietes structurales, elastiques et electroniques des perovskites AXO_3 (A=Sr,Bi,Na,K) par la methode (FP-LAPW).* PhD thesis, (2015).

[133] F Bowman. *Introduction to Bessel functions*. Courier Corporation, 2012.

[134] OK Andersen. Linear methods in band theory. *Physical Review B*, 12(8):3060, (1975).

[135] DD Koelling and GO Arbman. Use of energy derivative of the radial solution in an augmented plane wave method: application to copper. *Journal of Physics F: Metal Physics*, 5(11):2041, (1975).

[136] DR Hamann. Semiconductor charge densities with hard-core and soft-core pseudopotentials. *Physical Review Letters*, 42(10):662, (1979).

[137] G Ovando, J Morales, and JL López-Bonilla. Three dimensional effective mass schrödinger equation: harmonic and morse-type potential solutions. *Journal of molecular modeling*, 19:2007–2014, (2013).

[138] DJ Singh. Adequacy of the local-spin-density approximation for gd. *Physical Review B*, 44(14):7451, (1991).

[139] S Goedecker and K Maschke. Alternative approach to separable first-principles pseudopotentials. *Physical Review B*, 42(14):8858, (1990).

[140] D Singh and H Krakauer. H-point phonon in molybdenum: Superlinearized augmented-plane-wave calculations. *Physical Review B*, 43(2):1441, (1991).

[141] DJ Singh and WE Pickett. Skutterudite antimonides: Quasilinear bands and unusual transport. *Physical Review B*, 50(15):11235, (1994).

[142] T Takeda and J Kubler. Linear augmented plane wave method for self-consistent calculations. *Journal of Physics F: Metal Physics*, 9(4):661, (1979).

[143] L Smrčka. Linearized augmented plane wave method utilizing the quadratic energy expansion of radial wave functions. *Czechoslovak Journal of Physics B*, 34(7):694–704, (1984).

[144] DJ Shaughnessy, GR Evans, and MI Darby. An improved LAPW method for the calculation of self-consistent electronic band structures. *Journal of Physics F: Metal Physics*, 17(8):1671, (1987).

[145] D Singh. Ground-state properties of lanthanum: Treatment of extended-core states. *Physical Review B*, 43(8):6388, (1991).

[146] P Blaha, K Schwarz, P Sorantin, and SB Trickey. Full-potential, linearized augmented plane wave programs for crystalline systems. *Computer physics communications*, 59(2):399–415, (1990).

[147] P Blaha, K Schwarz, KHG Madsen, D Kvasnicka, J Luitz, et al. wien2k. *An augmented plane wave+ local orbitals program for calculating crystal properties*, (2001).

[148] MW Lufaso and PM Woodward. Prediction of the crystal structures of perovskites using the software program spuds. *Acta Crystallographica Section B: Structural Science*, 57(6):725–738, (2001).

[149] YP Liu, HR Fuh, and YK Wang. Study of the half-metallic materials double perovskites Sr_2ZnBO_6 (B=Tc,Re,Ru,Os,Co,Pd,andAu) via first-principle calculations. *Journal of magnetism and magnetic materials*, 341:25–29, 2013.

[150] Y Izumiyama, Y Doi, M Wakeshima, Y Hinatsu, A Nakamura, and Y Ishii. Magnetic and calorimetric studies on ordered perovskite Ba_2ErRuO_6. *Journal of Solid State Chemistry*, 169(1):125–130, (2002).

[151] FD Murnaghan. The compressibility of media under extreme pressures. *Proceedings of the national academy of sciences of the United States of America*, 30(9):244, (1944).

[152] F Birch. Finite elastic strain of cubic crystals. *Physical review*, 71(11):809, (1947).

[153] W Guenez, A Bouguerra, I Touaibia, and F Chemam. Giant magneto optical properties in the double perovskites $Ba_2B'RuO_6$ (B'=Er,Tm). *Journal of Physics: Condensed Matter*, 34(50):505501, (2022).

[154] W Guenez, S Boudiba, and F Chemam. Structural, electronic, magnetic, and optical properties of a novel double perovskite Ba_2GdRuO_6. *Physica Scripta*, 98(5): 055913, (2023).

[155] A Menedjhi, N Bouarissa, S Saib, and K Bouamama. Halide double perovskite $Cs_2AgInBr_6$ for photovoltaic applications: Optical properties and stability. *Optik*, 243:167198, (2021).

[156] TJ Jacobsson, M Pazoki, A Hagfeldt, and T Edvinsson. Goldschmidt rules and strontium replacement in lead halogen perovskite solar cells: theory and preliminary experiments on $CH_3NH_3SrI_3$. *The Journal of Physical Chemistry C*, 119(46):25673–25683, (2015).

[157] A Menedjhi, N Bouarissa, S Saib, M Boucenna, and F Mezrag. Band structure and optical spectra of double perovskite $Cs_2AgBiBr_6$ for solar cells performance. *Acta Physica Polonica A*, 137(4):486, (2020).

[158] S Berri, D Maouche, F Zerarga, and Y Medkour. Ab initio study of the structural, electronic, elastic and magnetic properties of Cu_2GdIn, Ag_2GdIn and Au_2GdIn. *Physica B: Condensed Matter*, 407(17):3328–3334, (2012).

[159] J Ding, L Wen, Y Liu, and Y Zhang. Origin of ferrimagnetism and the effect of octahedral tilting in double-perovskite compound Sr_2CoRuO_6. *Journal of Magnetism and Magnetic Materials*, 535:168035, (2021).

[160] U Qazi, S Mehmood, Z Ali, I Khan, and I Ahmad. Electronic structure and magnetic properties of the perovskites $SrTMO_3$(TM=Mn,Fe,Co,Tc,Ru,Rh,Re,OsandIr). *Physica B: Condensed Matter*, 624:413361, (2022).

[161] M Getzlaff. *Fundamentals of magnetism*. Springer Science & Business Media, (2007).

[162] M Arejdal, M Kadiri, A Abbassi, A Slassi, A Ait Raiss, L Bahmad, and A Benyoussef. Magnetic properties of the double perovskite Ba_2CoUo_6: ab initio method, mean field approximation, and monte carlo study. *Journal of Superconductivity and Novel Magnetism*, 29:2659–2667, (2016).

[163] Y Doi, Y Hinatsu, K Oikawa, Y Shimojo, and Y Morii. Magnetic and neutron diffraction study on ordered perovskites Sr_2LnRuO_6 (Ln=Tb,Ho). *Journal of alloys and compounds*, 323:455–459, (2001).

[164] A Dal Corso, S Baroni, and R Resta. Density-functional theory of the dielectric constant: Gradient-corrected calculation for silicon. *Physical Review B*, 49(8):5323, (1994).

[165] M Alouani and JM Wills. Calculated optical properties of si, ge, and gaas under hydrostatic pressure. *Physical Review B*, 54(4):2480, (1996).

[166] A Dar, R Sharma, V Srivastava, and UK Sakalle. Investigation on the electronic structure, optical, elastic, mechanical, thermodynamic and thermoelectric properties of wide band gap semiconductor double perovskite Ba_2InTaO_6. *RSC advances*, 9(17):9522–9532, (2019).

[167] Mark Fox. *Optical properties of solids*. (2002).

[168] T Bellakhdar, Z Nabi, B Bouabdallah, B Benichou, and H Saci. Ab initio study of structural, electronic, mechanical and optical properties of the tetragonal $Cs_2AgBiBr_6$ halide double perovskite. *Applied Physics A*, 128(2):1–12, (2022).

[169] M Hussain, M Rashid, A Ali, MF Bhopal, and AS Bhatti. Systematic study of optoelectronic and transport properties of cesium lead halide (Cs_2PbX_6; X=Cl,Br,I) double perovskites for solar cell applications. *Ceramics International*, 46(13):21378–21387, (2020).

[170] M Nabi and DC Gupta. Small-band gap halide double perovskite for optoelectronic properties. *International Journal of Energy Research*, 45(5):7222–7234, (2021).

[171] S Guo, Q Zhang, R Sa, and D Liu. Exploring the stability and physical properties of double perovskite Cs_2SnI_6 by doping the Cl/Br atom: a dft study. *Computational and Theoretical Chemistry*, page 113609, 2022.

[172] S Al-Qaisi, H Rached, TA Alrebdi, S Bouzgarrou, D Behera, SK Mukherjee, M Khuili, M Adam, AS Verma, and M Ezzeldien. Study of mechanical, optical, and thermoelectric characteristics of Ba_2XMoO_6 (X=Zn,Cd) double perovskite for energy harvesting. *Journal of Computational Chemistry*, (2023).

[173] JA Abraham, D Behera, K Kumari, A Srivastava, R Sharma, and SK Mukherjee. A comprehensive dft analysis on structural, electronic, optical, thermoelectric, slme properties of new double perovskite oxide Pb_2ScBiO_6. *Chemical Physics Letters*, 806:139987, (2022).

[174] T Lantri, S Bentata, B Bouadjemi, W Benstaali, B Bouhafs, A Abbad, and A Zitouni. Effect of coulomb interactions and hartree-fock exchange on structural, elastic, optoelectronic and magnetic properties of Co_2MnSi heusler: A comparative study. *Journal of magnetism and magnetic materials*, 419:74–83, (2016).

[175] HJ Kulik. Perspective: Treating electron over-delocalization with the dft+u method. *The Journal of chemical physics*, 142(24):240901, (2015).

[176] C Loschen, J Carrasco, KM Neyman, and Francesc Illas. First-principles lda+u and gga+u study of cerium oxides: dependence on the effective u parameter. *Physical Review B*, 75(3):035115, (2007).

[177] T Usman, G Murtaza, H Luo, and A Mahmood. Gga and gga+u study of rare earth-based perovskites in cubic phase. *Journal of Superconductivity and Novel Magnetism*, 30(6):1389–1396, (2017).

[178] Y Okamura, S Minami, Y Kato, Y Fujishiro, Y Kaneko, J Ikeda, J Muramoto, R Kaneko, K Ueda, and V Kocsis. Giant magneto-optical responses in magnetic weyl semimetal $Co_3Sn_2S_2$. *Nature communications*, 11(1):1–8, (2020).

[179] W Feng, GY Guo, J Zhou, Y Yao, and Q Niu. Large magneto-optical kerr effect in noncollinear antiferromagnets Mn_3X(X=Rh,Ir,Pt). *Physical Review B*, 92(14): 144426, (2015).

[180] JL Erskine and EA Stern. Magneto-optic kerr effects in gadolinium. *Physical Review B*, 8(3):1239, (1973).

[181] J Cai, X Tao, W Chen, X Zhao, and M Tan. Density-functional theory calculations on the magneto-optical kerr effects in Co_2TiSn and Co_2ZrSn. *Journal of magnetism and magnetic materials*, 292:476–482, (2005).